AN ABSTRACT OF THE THESIS OF

Annika Magnuson O'Dea for the degree of Master of Science in Civil Engineering presented on September 18, 2014.

Title: On the Nearshore Impact of Wave Energy Converter Arrays

Abstract Approved:

_____

Merrick C. Haller

Radiation stresses, defined as the excess flow of momentum due to the presence of waves (Longuet-Higgins, 1964), are the main drivers behind the cross-shore and longshore forcing that results in wave setup, set-down, and longshore currents (e.g. Svendsen, 2006). Longshore currents entrain and transport sediment and therefore play an important role in short- and long-term coastal evolution (Komar, 1998). Due to their importance in many nearshore processes, quantifying and analyzing nearshore radiation stresses is often an important component of coastal engineering and management projects.

This thesis presents two manuscripts focusing on radiation stress in nearshore zones. The first manuscript describes a methodology for assessing the nearshore impacts of the presence of Wave Energy Converter (WEC) arrays based on the net change in the alongshore radiation stress gradients shoreward of the array. First, a threshold for nearshore hydrodynamic impact is established based on the observed relationship between nearshore radiation stress and the maximum alongshore current velocity in past field studies. A parametric study is then conducted on an idealized beach using the spectral model SWAN to analyze nearshore impact using a range of array configurations, locations, and incident wave conditions. WEC devices are represented in SWAN through the external modification of the wave spectra at the device location using an experimentally determined power transfer function. In the final section, the same methodology is applied to two wave energy test sites off the coast of Oregon to assess the applicability of the conclusions made in the parametric study to sites with more complicated bathymetries. Although the changes in wave height, wave direction, and cross-shore force in the lee of the array are similar to the changes seen in

the parametric study, the changes in longshore radiation stress forcing are more heavily influenced by local bathymetry.

The second manuscript examines how the total radiation stress is affected by directional asymmetry in the incident wave spectrum. The process of wave refraction in nearshore zones results in an asymmetric directional distribution of spectral energy when oblique, multi-directional wave fields propagate into shallow water areas with limited alongshore variability. In this study, net radiation stresses are calculated using a JONSWAP frequency spectrum with both symmetric and asymmetric directional spreading functions and then compared to those calculated from the monochromatic formulation. Because information on the full frequency and directional distribution of spectral energy is not always available in practice, the monochromatic formulation is often used as an approximation of the true radiation stress. Past studies have demonstrated that the use of the monochromatic approximation in radiation stress calculations results in a significant overestimation of the radiation stress components S_{xx} and S_{xy} in broad-banded seas. The present results show that the inclusion of directional asymmetry in radiation stress calculations reduces the difference between the full spectral S_{xx} and the monochromatic approximation but increases the difference between the full spectral S_{xy} and the monochromatic approximation for a range of dominant wave directions. The use of a monochromatic approximation of S_{xy} can therefore lead to an overestimation of the actual radiation stress in certain sea states and consequently an overestimation of associated parameters such as alongshore current velocities and alongshore sediment transport rates.

On the Nearshore Impact of Wave Energy Converter Arrays

by
Annika Magnuson O'Dea

A THESIS

submitted to

Oregon State University

in partial fulfillment of
the requirements for the
degree of

Master of Science

Presented September 18, 2014
Commencement June 2015

Master of Science thesis of Annika Magnuson O'Dea presented on September 18, 2014.

APPROVED:

_____

Major Professor, representing Civil Engineering

_____

Head of the School of Civil and Construction Engineering

_____

Dean of the Graduate School

I understand that my thesis will become part of the permanent collection of Oregon State University libraries. My signature below authorizes the release of my thesis to any reader upon request.

_____

Annika Magnuson O'Dea, Author

ACKNOWLEDGEMENTS

This material is based upon work supported by the Department of Energy under Award Number DE-FG36-08GO18179. I would like to acknowledge and thank the Northwest National Marine Renewable Energy Center (NNMREC) and the Oregon Sea Grant for their support of this research.

I would also like to thank Gabriel Garcia-Medina for providing the Pacific Northwest hindcast data used as input conditions in the real test sites, as well as Ed Dever, Craig Risien, and the Ocean Observatories Initiative for providing the AWAC data used in model validation.

Lastly, I would like to thank my advisor, Merrick Haller, for his time, input, and support over the last two years, along with my remaining committee members, Peter Ruggiero, Tuba Özkan-Haller, and Emily Shroyer for their feedback. Finally, I would like to thank Gabriel Garcia-Medina (again) for all of his help along the way.

CONTRIBUTION OF AUTHORS

In the first manuscript, Merrick Haller provided guidance in the project orientation, design, and analysis, and assisted in the organization and readability of the manuscript. Tuba Özkan-Haller provided input and feedback in project design, progress, and analysis. In the second manuscript, Merrick Haller provided the initial motivation for the project and assisted with the interpretation of the results. He also gave feedback on the organization and readability of the manuscript.

TABLE OF CONTENTS

Page

Introduction …… 1

The Impact of Wave Energy Converter Arrays on Nearshore Wave Forcing …….. 3

Abstract …… 4

1. Introduction…… 5
2. Threshold for Nearshore Impact …… 7
3. Parametric Study of Impact …… 10
4. Nearshore Impact at Field Sites …….. 16
5. Conclusions …… 20

Acknowledgements …… 20

Figures …… 22

Tables …… 37

References …… 39

A Note on the Effect of Asymmetric Directional Spreading on the Total Radiation Stress... 41

Abstract …… 42

1. Introduction …… 43
2. Methods …….. 45
3. Results and Discussion …… 49
4. Conclusions …… 51

Figures …… 52

Tables …… 55

References …….. 57

Combined References ……..59

Appendices …….. 62

Appendix A: Directional Resolution …… 63

Appendix B: Extended results from parametric study. ……..… 67

Appendix C: Hindcast analysis and input conditions for NNMREC trials …… 75

Appendix D: SWAN domain of the continental shelf, with local bathymetry…….. 81

Appendix E. Extended results on the importance of directional asymmetry in the calculation of radiation stress values……...82

LIST OF FIGURES

Figure Page

Manuscript 1: The Impact of Wave Energy Converter Arrays on Nearshore Wave Forcing

1. Figure 1. a) S_{xy}/ρ at the 6.5 m contour line and b) the F_y at the location of maximum dissipation as a function of H_{rms} and θ ……..22

2. Figure 2. Model bathymetry for cases with an array located a) 5 km from shore, b) 10 km from shore, and c) 15 km from shore…….…....23

3. Figure 3. The experimentally determined PTF as a function of wave frequency (Rhinefrank et al., 2013) …… 24

4. Figure 4. Differences in **a)** H_s (left) in the lee of a widely-spaced array, **b)** θ in the lee of a widely-spaced array, **c)** H_s (left) in the lee of a closely-spaced array, and **d)** θ in the lee of a closely-spaced array from trials with an input H_s = 6 m, an input T_p = 12 s, low directional spread (14^0), and an array located 15 km from shore. …….25

5. Figure 5. Differences in **a)** H_s (left) in the lee of a widely-spaced array, **b)** θ in the lee of a widely-spaced array, **c)** H_s (left) in the lee of a closely-spaced array, and **d)** θ in the lee of a closely-spaced array from trials with an input H_s = 6 m, an input T_p = 12 s, high directional spread (35^0), and an array located 15 km from shore. ……26

6. Figure 6. Longshore H_s transects in the lee of a closely-spaced array located a) 5 km and b) 10 km offshore, as well as a widely-spaced array located c) 5 km and d) 15 km offshore with an input H_s = 6 m, an input T_p = 12 s, and low directional spread (14^0)…….…….. 27

7. Figure 7. Longshore F_y transects in the lee of a closely-spaced array located a) 5 km, b) 10 km, and c) 15 km from shore with an input H_s = 6 m, an input T_p = 12 s, and low directional spread (14^o)..……...……...28

8. Figure 8. Longshore F_y transects in the lee of a widely-spaced array located a) 5 km, b) 10 km, and c) 15 km from shore with an input H_s = 6 m, an input T_p = 12 s, and low directional spread (14^o) ……...…...29

9. Figure 9. Location of the NETS site (in black), the SETS site (in blue), and the AWAC used in model validation (in red)…….....…….. 30

10. Figure 10. Model bathymetry for simulations at a) the NETS site and b) the SETS site...31

11. Figure 11. Significant wave height from the processed AWAC data (black) and the SWAN trials (red) for the duration of the AWAC deployment period (March to August 2011) ……..... 32

LIST OF FIGURES (Continued)

Figure Page

12. Figure 12. Difference in significant wave height in the lee of **a)** a closely-spaced array and **b)** a widely-spaced array at the SETS site for trials with an input H_s = 5.45 m, an input T_p = 12.61 s, and an input θ = -27.11^0…… 33

13. Figure 13. Input H_s and T_p from **a)** all trials at the SETS site, **b)** all trials at the SETS site when the location of the jetties and Yaquina Head have been excluded from the analysis, and **c)** all trials from the NETS sites…… 34

14. Figure 14. Longshore F_y transects in the lee of **a)** a closely-spaced array and **b)** a widely-spaced array (bottom) at the SETS site for trials with an input H_s = 5.45 m, an input T_p = 12.61 s, and an input θ = -27.11^0.....35

15. Figure 15. Difference in significant wave height in the lee of **a)** a closely-spaced array and **b)** a widely-spaced array at the NETS site for trials with an input H_s = 5.45 m, an input T_p = 12.61 s, and an input θ = -27.11^0..…….……... 36

Manuscript 2: A Note on the Effect of Asymmetric Directional Spreading on the Total Radiation Stress

16. Figure 1. $G(f,\theta)$ at the peak frequency (f_p = 0.0934) from trials with high directional spread (offshore s_{max} = 10) as a function of wave direction with an offshore dominant wave direction of a) 30^0 and b) 60^0. 52

17. Figure 2. Frequency directional spectra $S(f,\theta)$ from cases with a) a symmetric spectrum and a 30^0 offshore dominant wave direction, b) an asymmetric spectrum and a 30^0 offshore dominant wave direction, c) a symmetric spectrum and a 60^0 offshore dominant wave direction, and d) an asymmetric spectrum and a 60^0 offshore dominant wave direction for high directional spread cases (offshore s_{max} = 10). ……53

18. Figure 3. Ratio of true to narrow-banded a) S_{xx} ($S_{xx}^{(tr)}/S_{xx}^{(nb)}$) and b) S_{xy} ($S_{xy}^{(tr)}/S_{xy}^{(nb)}$) as a function of dominant offshore wave direction for both cases with high (offshore s_{max} = 10) and low (offshore s_{max} = 75) directional spread..…… 54

LIST OF TABLES

Table Page

Manuscript 1: The Impact of Wave Energy Converter Arrays on Nearshore Wave Forcing

1. Table 1. Input conditions for all trials in the parametric study ……..……37

2. Table 2. Results from trials with an array located 5 km from shore……..……38

Manuscript 2: A Note on the Effect of Asymmetric Directional Spreading on the Total Radiation Stress

3. Table 1. Input conditions for all trials. ……...55

4. Table 2. Input conditions, conditions at the 10 m contour line, and narrow-banded radiation stress values from all trials.……..….56

LIST OF APPENDIX FIGURES

Figure Page

Appendix A: Directional Resolution

1. Figure 1. Longshore transects of the difference in F_y at the location of maximum dissipation for trials with increasing directional resolution, from 72 directional bins to 900 directional bins……..…….63-65

2. Figure 2. Filtered longshore transects of the difference in F_y at the location of maximum dissipation for trials with increasing directional resolution, with a) a closely-spaced array and b) a widely-spaced array…….……. 66

Appendix B: Extended results from parametric study.

3. Figure 1. Longshore F_x transects in the lee of a closely-spaced array located a) 5 km and b) 10 km from shore with an input H_s = 6 m, an input T_p = 12 s, and low directional spread (14^0)…… 73

4. Figure 2. Longshore F_x transects in the lee of a widely-spaced array located a) 5 km and b) 10 km from shore with an input H_s = 6 m, an input T_p = 12 s, and low directional spread (14^0) ……..…. 74

Appendix C. Hindcast analysis and input conditions for NNMREC trials.

5. Figure 1. Two dimensional histogram of significant wave height and mean wave direction……..…… 75

6. Figure 2. Two dimensional histogram of significant wave height and peak period…...… 76

7. Figure 3. Two dimensional histogram of mean wave direction and peak period……..…. 77

Appendix D. SWAN domain of the continental shelf, with local domain bathymetry

8. Figure 1. SWAN domain of the continental shelf…….……..81

LIST OF APPENDIX TABLES

Table Page

Appendix B: Extended results from parametric study.

1. Table 1. Results from trials with a widely-spaced array located 5 km from shore…….67
2. Table 2. Results from trials with a closely-spaced array located 5 km from shore. …….. 68
3. Table 3. Results from trials with a widely-spaced array located 10 km from shore……...69
4. Table 4. Results from trials with a closely-spaced array located 10 km from shore..…… 70
5. Table 5. Results from trials with a widely-spaced array located 15 km from shore…..….71
6. Table 6. Results from trials with a closely-spaced array located 15 km from shore……. 72

Appendix C. Hindcast analysis and input conditions for NNMREC trials.

7. Table 1. Input conditions and calculated centroids for the NNMREC trials…….78-80

Appendix E. Extended results on the importance of directional asymmetry in the calculation of radiation stress values

8. Table 1. Input conditions and resulting radiation stress values for all trials in the study...82

On the Nearshore Impact of Wave Energy Converter Arrays

Introduction

The nearshore zone is defined as the area from the shoreline to where waves are no longer influenced by the seabed. It is a complex region with distinct hydrodynamic processes (Svendsen, 2006). Nearshore processes include wave transformation and breaking, wave-induced set-up and set down, and nearshore circulation (e.g. rip currents and alongshore currents). These processes play a large role in the entrainment and transport of sediment and therefore significantly influence coastal morphology and coastal evolution (Komar, 1998).

Despite the importance of nearshore zones, the forces driving nearshore processes were poorly understood until Longuet-Higgins and Stewart proposed the concept of radiation stresses, defined as the excess flow of momentum due to the presence of waves, in a series of articles in the 1960s (Longuet-Higgins and Stewart, 1960; Longuet-Higgins and Stewart, 1964). Although the authors gave several examples of the importance of radiation stress in these articles, most notably as a driver of wave-induced set-up, it was not until 1970 that the application of radiation stress in the generation of longshore currents was proposed (Longuet-Higgins, 1970). Radiation stress forcing has since become recognized as an important factor in the generation of many wave-induced nearshore processes (Svendsen, 2006).

This thesis presents two studies focusing on the quantification and analysis of radiation stresses in nearshore zones. In the first study, the nearshore impact of Wave Energy Converter (WEC) arrays is assessed through the changes in radiation stress forcing shoreward of the array. A threshold radiation stress and associated longshore force value is established, and then this threshold is used to identify the array configurations, locations, and incident wave conditions that are most likely to significantly impact nearshore processes. In the second study, the importance of the inclusion of a refracted energy spectrum in the calculation of nearshore radiation stresses is analyzed. As oblique, multi-directional wave fields propagate into shallow water, the process of wave refraction results in an asymmetric distribution of spectral energy around the peak direction. In this study, the net radiation stresses are calculated using a JONSWAP frequency spectrum with both a symmetric and asymmetric directional spreading function to investigate the importance of this directional asymmetry in the calculation of radiation stress values. Both radiation stress values are then compared to radiation stress values calculated using the commonly-used monochromatic

formulation. Finally, the importance of directional asymmetry in nearshore radiation stress calculations is discussed, along with the implications of the use of monochromatic approximations or symmetric spectra in the calculation of radiation stress for coastal engineering projects.

The Impact of Wave Energy Converter Arrays on Nearshore Wave Forcing

Annika O'Dea

Merrick C. Haller

Tuba Özkan-Haller

Journal: *Coastal Engineering*

201 Mission Street
26th Floor
San Francisco, CA 94105

To be submitted 2014

Abstract

A new threshold for nearshore hydrodynamic impact due to the presence of Wave Energy Converter (WEC) arrays is defined based on the net change in the alongshore radiation stress gradients in the lee of the array. The minimum level for impact is established based on the observed relationship between the nearshore radiation stress and the alongshore current magnitude found in existing field data. Next, a parametric study is conducted on an idealized beach using the spectral model SWAN to analyze the nearshore impact of a suite of WEC array designs. WEC devices are represented in SWAN through the external modification of the wave spectra at the device location using an experimentally determined power transfer function. A range of WEC array configurations, locations, and incident wave conditions are examined and the limited set of wave conditions and array characteristics that generate alongshore gradients exceeding the previously established threshold are identified. In the final section, the same methodology is applied to two wave energy test sites off the coast of Oregon, USA, to assess the applicability of the conclusions made in the parametric study to sites with more complicated bathymetries. Although the changes in wave height, wave direction, and cross-shore force in the lee of the array are similar to the changes seen in the parametric study, the changes in longshore force are more heavily influenced by local bathymetry.

1. Introduction

For the exploitation of wave energy to be commercially viable, wave energy converters (WECs) will need to be deployed in arrays that include several to hundreds of individual devices. Understanding the potential impacts of WEC arrays on marine ecosystems and the coastal environment is crucial in order to ensure the sustainability and success of the nascent marine energy industry. Since most WEC designs are targeted for offshore sites (depths $\geq$ 50 m), potential nearshore effects arrive via the modified wave field created in the lee of a WEC array.

Interactions between WEC devices and the incident wave field can be separated into interactions that modify the wave field within the array (near-field interactions) and wave transformations that alter the wave climate in the lee of the array (far-field effects). The far-field effects of WEC arrays include a redirection of waves and a reduction in wave height in the lee of the array, referred to as the wave shadow. The extent and significance of the far-field effects of WEC arrays are a function of the array design, its location, and the incident wave conditions. Quantifying the changes in the far-field wave conditions as a result of WEC arrays is the first step in determining whether the WEC arrays will influence nearshore processes.

The far-field effects of WEC arrays have been investigated using spectral models (primarily SWAN) in a number of past studies. Most studies represent the array as single or multiple partially transmissible objects with a frequency-independent transmission coefficient (Millar et al., 2007; Rusu and Soares, 2013; Carballo and Iglesias, 2013; Abanades et al., 2014a and 2014b; and Iglesias and Carballo, 2014). However, the representation of devices or arrays as barriers with a frequency-independent transmission coefficient fails to capture the frequency-dependent energy extraction characteristics that are inherent to WEC devices. The amount of energy that real devices extract is a function of the device's power transfer function (PTF), defined as the proportion of available wave power extracted at each frequency by a particular device. Smith et al. (2012) altered the SWAN source code to allow for a frequency-dependent extraction of energy using a hypothetical PTF to assess the far-field effects of WEC arrays in the UK. Here, WEC devices are represented in SWAN through the external modification of the wave spectra at the device location using an experimentally-determined frequency dependent PTF established in an earlier laboratory study (Rhinefrank et al., 2013).

Although a few recent studies on far-field effects of WEC arrays have coupled spectral wave models with current or sediment transport models (Rusu and Soares, 2013; Gonzalez-Santamaria et al., 2013; Mendoza et al., 2014, Abanades et al., 2014a, Abanades et al., 2014b), most studies focus on the differences in wave height (or wave power) and direction in the lee of the array (Millar et al., 2007; Carballo and Iglesias, 2013; Palha et al., 2010; Smith et al., 2012; and Iglesias and Carballo, 2014). While changes in wave height and direction imply a change in nearshore forcing, the forcing terms in the nearshore hydrodynamic balance are more directly quantified through the spatial gradients in radiation stress (Svendsen, 2006). These gradients drive longshore currents, rip currents, and nearshore sediment transport. This study aims to assess nearshore impacts through a direct analysis of these nearshore forcing parameters.

Several approaches have been proposed in efforts to quantify and parameterize nearshore impact. Iglesias and Carballo (2014) assessed nearshore impact through the definition of several impact indicators based on changes in wave power at a defined contour. Similar to the previously discussed studies, this approach focuses exclusively on changes in wave power (a function of wave height), and therefore does not include potential changes in wave forcing. In a different approach, Abanades et al. (2014b) modeled the response of a beach to storm conditions both with and without a WEC array using a coupled wave propagation model and coastal processes model. To analyze and interpret the observed differences in beach response, they defined four impact indicators based on changes in bed level and erosions rates. The Iglesias and Carballo study provides a more thorough, yet computationally intense and site-specific, approach to the quantification of nearshore impact. In the present study, we propose a new threshold for hydrodynamic impact based on changes in nearshore forcing parameters. This threshold provides a computationally inexpensive method of quantifying and assessing nearshore impact.

The impacts of WEC arrays will ultimately depend on the characteristics of the array (number of devices, array configuration, and distance from shore) and the characteristics of the site (wave climate, bathymetry). However, the use of generalized descriptions of the impacts of WEC arrays as basic guidelines in the design process would allow for a more rapid assessment of candidate sites. One goal of this study is assess nearshore impacts of WEC arrays on a generic nearshore configuration in order to draw general conclusion that could be used to facilitate the preliminary design and development of future arrays.

This study can be separated into three parts. The objective of the first part is to determine a representative threshold alongshore force F_y level based on existing radiation stress and current field data that helps link changes in the wave climate to changes in nearshore processes. The objective of the second part is to determine how array spacing and distance from shore influence nearshore forcing, and to determine which array designs and incident wave conditions generate longshore forces that exceed the F_y threshold established in the previous section. The objective of the final part is conduct a similar assessment of real wave energy sites in order to determine whether the general conclusions made in the idealized study are valid in field sites with more complicated bathymetries.

2. Threshold for Nearshore Impact

The extraction of wave energy by WEC devices results in changes in both the wave height and direction in the lee of the array. Changes in wave parameters such as wave height and direction alter the wave-induced radiation stresses, defined as the excess flux of momentum due to the presence of waves (Longuet-Higgins et al., 1964). The spectral wave model SWAN was used to simulate wave transformation in the lee of WEC arrays and to calculate the cross-shore and alongshore wave radiation stress gradients.

2.1 Model overview

SWAN is a third-generation spectral wave model (Booij et al., 1999) and uses the spectral action balance equation to calculate the transformation of wave spectra in nearshore processes. The spectral action balance is shown in Equation 1,

$$\frac{\partial N}{\partial t} + \frac{\partial c_x N}{\partial x} + \frac{\partial c_y N}{\partial y} + \frac{\partial c_\sigma N}{\partial \sigma} + \frac{\partial c_\theta N}{\partial \theta} = S_{tot} \quad (1)$$

where N is the energy density, c_x and c_y are the velocity components of N in geographical space, θ is the wave direction, σ is the relative frequency, and c_σ and c_θ are the propagation velocities of N in σ- and θ-space. The term S_{tot} represents the sum of the physical processes that result in the generation, redistribution, and dissipation of energy. These processes include wave growth through energy transfer from wind (energy generation), nonlinear transfer of wave energy through quadruplet and triad interactions (energy redistribution), as well as the loss of energy through wave breaking, bottom friction, and white-capping (energy

dissipation). In this study, only depth-induced breaking was included from this list of physical processes.

The process of wave diffraction, the lateral spreading of energy in the direction perpendicular to wave propagation (Dean and Dalrymple, 2010), is not accounted for in phase-averaged models such as SWAN. Diffraction can be approximated by SWAN through the use of a phase-decoupled refraction-diffraction approximation (Holthuijsen et al., 2003). The spatial resolution used in this model was finer than the suggested resolution for the activation of diffraction, (SWAN team, 2006a.), and the model did not converge when diffraction was activated. For this reason, the diffraction approximation was not used in this study.

2.2 Wave forcing

Radiation stresses are the main drivers behind the cross-shore and longshore forces that result in wave setup, set-down, and longshore currents (Svendsen, 2006). The depth-averaged, steady state formulations for wave-induced forces in the cross-shore (F_x) and the longshore (F_y) direction used in SWAN are shown in Equations 2 and 3, respectively,

$$F_x = -\frac{dS_{xx}}{dx} - \frac{dS_{xy}}{dy} \tag{2}$$

$$F_y = -\frac{dS_{yx}}{dx} - \frac{dS_{yy}}{dy} \tag{3}$$

where S_{xx}, S_{xy}, $S_{yx,}$ and S_{yy} are the radiation stress terms (SWAN team, 2006b.). The radiation stress terms are a function of both wave energy (and therefore the square of the wave height), wave direction, wave number, and water depth. The linear water wave approximation of these terms are shown in Equations 4, 5, and 6,

$$S_{xx} = E[n(\cos^2\theta + 1) - \tfrac{1}{2}] \tag{4}$$

$$S_{yy} = E[n(\sin^2\theta + 1) - \tfrac{1}{2}] \tag{5}$$

$$S_{xy} = S_{yx} = \tfrac{E}{2} n sin2\theta \tag{6}$$

where E is the wave energy, θ is the wave direction, k is the wave number, and h is the water depth, and with n given by Equation 7 (Svendsen, 2006).

$$n = \frac{1}{2}\left(1 + \frac{2kh}{sinh2kh}\right) \quad (7)$$

Although the nearshore force is a function of the spatial gradient in radiation stress, Guza et al. (1986) and Feddersen et al. (1998) have empirically demonstrated that a strong correlation exists between the radiation stress S_{xy} at a fixed point outside the surf zone and the maximum longshore current velocity. Guza et al. (1986) collected their data during the Nearshore Sediment Transport Study (NSTS) at Leadbetter Beach, Santa Barbara, CA from January through February 1980. The data show an approximately linear relationship between S_{xy}/ρ measured outside the surf zone (at approximately the 6.5 m depth contour) and the observed longshore current velocity (Guza et al., 1986, see Figure 12). Here, we define 20 cm/s as a threshold longshore current magnitude, with currents above 20 cm/s considered significant. This longshore current value translates to a threshold $S_{xy}/\rho g$ value of approximately 32 cm^2 (at the 6.5 m contour line) using the Guza et al. (1986) data.

Again, we note that Equations (2) and (3) show that the nearshore forcing terms are not directly dependent on the radiation stress magnitudes, but on their spatial gradients. Specifically, the cross-shore gradient of S_{xy} is the dominant forcing term in the total longshore forcing F_y on an alongshore uniform slope. Hence, in order to relate the longshore current threshold to a threshold of the longshore forcing F_y, we ran a set of simulations using SWAN over a generic planar beach and compared the resulting S_{xy} and F_y values. The beach had a slope of 1:25, chosen to roughly match the average measured slope at Leadbetter Beach during the data collection period (Guza et al., 1986). The simulations use a range of significant wave heights (0.5 m to 6 meters) and dominant wave directions (0° to 45°). The radiation stress was calculated using Equations 4-6 at the 6.5 m contour line (chosen to match the location of the S_{xy} measurement at Leadbetter Beach), using the significant wave height calculated in SWAN and the remaining parameters determined using linear wave theory. The longshore force F_y was calculated by SWAN and was assessed at the breaking point, defined in this study as the location of maximum dissipation.

The resulting radiation stress S_{xy} and longshore force F_y from the threshold F_y trials were plotted as a function of root mean square wave height H_{rms} and the mean wave direction θ (Figure 1). Both S_{xy} and F_y showed an increase in magnitude with either an increase in H_{rms} or an increase in θ. The $S_{xy}/\rho g$ = 32 cm^2 contour line was plotted on both figures, shown in red. By finding the F_y contour that most closely matches the $S_{xy}/\rho g$ = 32 cm^2 contour line, we

were able to map the significant $S_{xy}/\rho g$ value to a significant F_y value, which was found to be 0.44 N/m^2. This value was used as a F_y threshold, and all changes in F_y (ΔF_y) that exceeded this threshold were considered significant enough to impact nearshore processes.

3. Parametric Study of Impact

3.1 Model domain

For the parametric study on the nearshore impacts of WEC arrays, we used a 24 km by 70 km model domain discretized into a regular grid with a spatial resolution of 200 m. Within this domain, four smaller, higher resolution grids were nested. The bathymetry was designed to be representative of a generic coastline with wave propagation starting in deep water. The domain consisted of an offshore section with a cross-shore length of 2 km and a constant depth of 400 m, followed by a 2 km section with a 1:10 slope, and finally a 20 km planar shelf with a slope of 1:100. The spatial resolution increased from 200 m in the largest grid to 50 m in a 20 km by 20 km nested grid. A spatial resolution of 9 m was used in the vicinity of the WEC array, followed by a spatial resolution of 18 m in the nearshore zone. WEC arrays were located either 5, 10, or 15 km offshore. The domain bathymetry showing the location and size of the nested grids is shown in Figure 2.

3.2 Model resolution

In SWAN, the wave action density spectrum is discretized into a given number of frequency and directional bins as defined by the user. Test trials were conducted with varying directional resolution to assess the number of directional bins necessary to resolve the effects of the individual WECs on the wave field. Trials were simulated with the same input significant wave height H_s (3 m), peak period T_p (12 s), mean wave direction θ (0^0), directional spread (14^0), and array location (10 km from shore) and with the wave action density spectra discretized into 72, 90, 120, 180, 360, 500, 720, and 900 directional bins. The H_s, θ, and longshore force outputs F_x and F_y were compared in the lee of the array. Spatially periodic variations were seen in the lee of the array in all three of the parameters analyzed. The length scale of the oscillations in the H_s, θ, F_x, and F_y were found to be dependent on resolution but to converge as the directional resolution increased. However, the magnitude of the oscillations did not converge in each of these parameters (particularly F_x, and F_y) as resolution increased. As a result, we chose to filter the output parameters using a 270 m

moving average. When filtered, the differences between the output parameters as a function of directional resolution disappeared. Examples of the oscillations in the output parameters in the lee of the array are shown in Appendix A, Figure1 for trials with 60 WECs location 10 km offshore. The filtered transects are shown in Appendix A, Figure 2.

Final trials were run with 720 directional bins. The wave action density spectrum was discretized logarithmically into 40 frequency bins (0.04118-0.5 Hz), which is consistent with the frequency spread and resolution used in other similar studies using SWAN.

3.3 Input conditions

All trials in the parametric study were simulated using JONSWAP spectra as input conditions at the offshore boundary. The effects of changes in significant wave height H_s, peak period T_p, and directional spread were assessed. Trials were conducted with two input significant wave heights (2 m and 6 m) and nine input peak periods (6, 7, 8, 9, 10, 12, 14, 16, and 18 s). All trials were conducted with a directional wave field with the dominant direction being shore normal. Two directional spreads were assessed, including a low directional spread case (14°) and a high directional spread case (35°). The average annual offshore directional spread on the Oregon coast was calculated from a 2011 WAVEWATCH III hindcast of the Pacific Northwest (Garcia-Medina et al., 2013), and this value was used as the low directional spread case. The high directional spread case was selected to be slightly higher than the SWAN default (30°), and within the range of directional spread values used in past studies on WEC arrays. A total of 36 sets of wave conditions were simulated. Trials were conducted with these input conditions using two array configurations (closely-spaced and widely-spaced) and with arrays located at three distances from shore (5, 10, and 15 km). Simulations were also made without an array for each set of input conditions. A total of 252 trials were conducted. Input conditions for all trials in the parameterized study are shown in Table 1.

3.4 Representation of WECS in SWAN

The PTF was determined in a previous laboratory study conducted using scaled versions of Columbia Power Technologies' Manta Buoy, a point absorber type WEC (Rhinefrank et al, 2013). The laboratory PTF was then scaled to have a peak period of

extraction at 9 s, which is the average annual energy period on the Oregon coast (Lenee-Bluhm, et al., 2011). The PTF as a function of wave frequency is shown in Figure 3.

The PTF represents the proportion of wave energy extracted across the diameter of a device as a function of frequency. Subtracting the PTF from 1 (at each frequency) therefore gives the proportion of wave energy remaining in the wave field after the device. As is evident from Figure 3, the measured PTF from the laboratory work exceeds one for a narrow range of frequencies. This is indicative of increased energy capture efficiency and is made possible through the process off wave diffraction. In order to capture this behavior in the model it would be necessary to artificially increase the device diameter. However, where the experimental PTF was greater than 1, we chose to cap the PTF at a value of 1, meaning the simulated WECs are slightly less efficient than the lab scale WECs. Wave spectra were externally modified at the device locations using Equation 8,

$$S_{after} = S_{before} * (1 - PTF) \tag{8}$$

where S_{before} is the spectral energy density in the wave field before the device and S_{after} is the spectral energy density in the wave field after the device.

Here we study large scale WEC arrays which included 60 devices in two staggered rows. Each device had a diameter of 18 m. To assess the importance of spacing between devices, both closely-spaced and widely-spaced arrays were simulated for each set of input wave conditions. Closely-spaced arrays had a distance of 72 m (4 times the WEC diameter) between devices and rows, and widely-spaced arrays had a distance of 180 m (10 times the WEC diameter) between devices and rows. Array spacing and configuration was selected based on past studies on optimal WEC array configurations (Beels, 2009; Beels 2010; Babarit, 2013).

3.5 Model outputs

For each trial, the significant wave height H_s, mean wave direction θ, peak period T_p, and the wave-induced forces F_x and F_y were calculated at each grid point across the domain. As a measure of nearshore impact, the difference in longshore force F_y across the domain with and without the array was determined and demeaned to focus on the spatial variability in F_y. Oscillations in H_s, θ, F_x, and F_y were seen in the lee of the array. The magnitude of these

oscillations was affected by the directional resolution used in the simulations, and did not appear to converge with an increase in directional resolution (see Section 3.2). Because of this, the resulting parameters were filtered in the lee of the array using 270 m spatial filter in both the cross-shore and longshore direction to focus on the broad changes in the wave field generated by the presence of the WEC array. Changes in H_s, F_x, and F_y in the surfzone were analyzed.

3.6 Model results

3.6.1 Changes in significant wave height H_s and mean wave direction θ

Figure 4 shows the differences in H_s, (left) and θ (right) in the lee of both widely-spaced (top) and closely-spaced (bottom) WEC arrays across the domain for trials with an input H_s = 6 m, an input T_p = 12 s, and 14^0 directional spread and with an array located 15 km from shore. The reduction in H_s and the redirection of waves due to the WEC array is clearly visible. The redirection of waves in the WEC shadow results in a positive change in direction to one side of the array and a negative change in direction to the other side of the array.

Both directional spread and the distance between the WEC and the shore were found to be important factors in the regeneration of waves in the lee of the array. When the WEC arrays were located closer to shore, the wave field had less distance for wave to regenerate and larger differences were seen in the surf zone between cases with and without arrays. The largest changes in all parameters were seen when the array was located 5 km from shore.

High directional spread was found to increase wave regeneration in the lee of the array. This resulted in a decrease in the magnitude of the change in H_s, but an increase in the longshore extent of the WEC shadow. The changes in θ in the direct lee of the array were found to be more significant in cases with high directional spread. The differences in wave regeneration in trials with low versus high directional spread are visible in plots of the difference in H_s and θ, shown in Figures 4 and 5, respectively (with an input H_s = 6 m, an input T_p = 12 s, and an array located 15 km from shore).

WEC array spacing played a significant role in the magnitude of the changes in H_s and θ in the lee of the array. When devices were closer together, much more significant change in both H_s and θ were seen in the immediate lee of the array (see Figures 4 and 5). As the waves regenerated in the lee of the array, the differences between cases as a function of array spacing decreased. The most significant differences in surfzone parameters between

cases as a function of array spacing were seen with low directional spread and when the array was located 5 km from shore.

Longshore H_s transects taken at the location of the maximum wave height (in the absence of an array) in the lee of a closely-spaced and a widely-spaced array are shown in Figures 6 (all with an input H_s = 6 m, an input T_p = 12 s, low directional spread (14^0), and arrays located 5 km and 15 km from shore). These figures allow an additional visualization of the changes in H_s seen in the difference plots shown in Figure 4. As expected, the decrease in H_s grows increasingly significant as the array moves toward the shoreline, particularly in the lee of a closely-spaced array. The maximum reduction in H_s in the lee of a closely-spaced array was 12.1 % when the array was 5 km from shore, 6.3 % when the array was 10 km from shore, and 3.4 % when the array was located 15 km from shore. The maximum reduction in H_s in the lee of a widely-spaced array was 6.0 % when the array was 5 km from shore, 4.8 % when the array was 10 km from shore, and 2.8 % when the array was located 15 km from shore. The maximum reduction in H_s was less than 6.3 % for all trials with high directional spread. Results are summarized in Appendix B, Tables 1-6.

In most cases, the most significant decreases in H_s were seen with trials with an input T_p of 9 or 10 s. As discussed in Section 3.4, the PTF was scaled to have a peak period of extraction of 9 s, meaning the largest percent of the available energy was extracted from the incident wave field at this period.

3.6.2 Changes in cross-shore force F_x

Cross-shore force F_x and longshore force F_y are dependent on the gradient of the wave-induced radiation stress, and are therefore strongest in the surf zone (Svendsen, 2006). The decrease in H_s in the lee of the array demonstrated in the previous section results in a similar decrease in the maximum magnitude of F_x. Longshore transects of F_x at the location of its maximum in the lee of a closely-spaced array and a widely-spaced array are shown in Appendix B, Figure 1 and 2, respectively (all with an input H_s = 6 m, an input T_p = 12 s, low directional spread (14^0), and arrays located 5 and 10 km from shore). Maximum F_x values for cases with and without arrays were compared, and the results are shown in Appendix B, Tables 1-6. A maximum reduction of 9.0 % was seen in the magnitude of F_x with an array 5 km from shore, and a maximum reduction of 3.0 % was seen in cases with an array located 15

km from shore. The maximum reduction in F_x was less than 5 % for all trials with high directional spread.

3.6.3 Changes in longshore force F_y

The longshore force F_y, similar to the cross-shore force F_x, is a function of the spatial gradient of the wave-induced radiation stresses, and is therefore strongest in the surf zone. Because F_y depends on the radiation stress component S_{xy}, its magnitude and direction are heavily influenced by the incident wave angle as it approaches the shore (Svendsen, 2006). The spatial variability in the direction of the incident waves due to the WEC array therefore has significant implications for the magnitude and orientation of F_y.

Using the filtered modeled results, the maximum changes in F_y (ΔF_y) at the location of maximum dissipation were found for all trials, and the results are shown in Table 2, with extended results shown in Appendix B, Table 1-6. Larger input H_s and T_p values were found to result in larger ΔF_y values in the surf zone. Only trials with an input H_s = 6 m and an input T_p greater than 7 s resulted in ΔF_y values over the established threshold. The trials that met the threshold ΔF_y value are summarized in Table 2.

Similar to the previously discussed parameters, the distance between the WEC array and the shore was found to have a significant impact on the magnitude the F_y generated in the surf zone. Less wave regeneration was possible in the lee of an array 5 km from shore, resulting in a more significant change in the magnitude of F_y in the surf zone for these cases. Only trials with an array located 5 km from shore generated F_y values over the established threshold (shown in Table 2). Although an increase in directional spread resulted in a decrease in the changes in H_s, significant changes in wave parameters in the surf zone were still seen in trials with high directional spread with an array located 5 km from shore. A total of 12 trials were found to meet the threshold F_y value, seven of which were from cases with low directional spread with the remaining five from cases with high directional spread (Table 2). The differences between cases as a function of directional spread increased as the array moved away from shore. Virtually no changes were seen in the wave field in cases with high directional spread and with an array located 10 or 15 km from shore (see Appendix B, Tables 3-6).

WEC array spacing had an effect on both the magnitude and the extent of the far-field changes. Closely-spaced arrays resulted in a significantly larger change in wave parameters in

the direct lee of the array (Figure 4). The magnitude of F_y at the location of maximum dissipation was found to be larger in the lee of closely-spaced arrays in all trials, but the differences between cases based on WEC spacing decreased with increasing distance from the array (Appendix B, Tables 1-6).

To visualize the spatial variability in F_y in the surf zone, longshore F_y transects were plotted at the location of maximum dissipation for trials with an input H_s = 6 m, an input T_p = 12 s, and low directional spread (14^0) (Figures 7 and 8). The difference in θ on either side of the array results in a similar spatial variability in the direction of F_y. The F_y vector on either side of the array is directed toward the area directly behind the array, resulting in a convergence of force in this area.

Oscillating F_y values were seen at the location of maximum dissipation in the direct lee of the array. Oscillating longshore forces can have significant impacts on nearshore processes and are especially important in the generation of rip currents (Bowen, 1969). Although these oscillations were present in all trials, the magnitude of these oscillations was found to depend on the model resolution, and did not converge with an increase in resolution. Although it was determined that these oscillations could not be adequately modeled with SWAN, it remains unclear whether these oscillations are entirely a numerical result of SWAN, or if they are indeed present. Determining whether these oscillations are realistic and if so determining their magnitude and importance are potential areas of future study.

4. Nearshore Impact at Field Sites

4.1 Model domain

To assess the applicability of the conclusions made in the parametric study to sites with more realistic bathymetries, the same methodology was applied to two Northwest National Marine Renewable Energy Center (NNMREC) test sites off the coast of Newport, OR, the North Energy Test Site (NETS) and the South Energy Test Site (SETS) (Figure 9).

The same 17 km by 75 km local domain was used for both the NETS site (located north of Yaquina Head, approximately 5 km offshore) at the SETS site (located south of Newport, approximately 11 km offshore) (Figure 9). Similar to the parametric study, the domain was discretized into a regular grid with a spatial resolution of 200 m. Within the domain, two sets of five smaller, higher resolution grids were nested, one for each site. Figure 10 shows these five nested grids for each site.

The domain bathymetry was generated using the 1/3 arc-second Central Oregon Coast Digital Elevation Map (DEM) from the National Geophysical Data Center (NDGC), part of the National Oceanic and Atmospheric Administration (NOAA). The domain was rotated 5 degrees so the coastline was approximately parallel to the offshore domain boundary and filtered using a 54 m low-pass filter in both the cross-shore and longshore direction. The spatial resolution increased from 200 m in the largest grid to 50 m in the first nested grid, followed by 30 m in the second nested grid. Similar to the parametric study, a spatial resolution of 9 m was used in the vicinity of the WEC array, followed by a spatial resolution of 18 m in the nearshore zone.

The wave action density spectra were discretized into 180 directional bins and 40 logarithmic frequency bins. WEC arrays were located approximately equidistant from the east and west permitted boundaries of the test sites, although the arrays extended beyond the north and south boundaries of the test sites.

4.2 Model validation

The SWAN model was validated using measured significant wave height values from an Acoustic Wave and Current Meter (AWAC) deployed within the model domain (Vardaro et al., 2011). The AWAC was deployed from March to August 2011 at a location just south of Yaquina Head (Figure 9). Validation trials were simulated using wave spectra from a WAVEWATCH III hindcast for the Pacific Northwest as input conditions (see Section 4.3 for hindcast details) (Garcia-Medina et al., 2013). Trials were simulated for each hour of the deployment period. The significant wave height measured by the AWAC was compared with the significant wave height calculated by SWAN at the device location. The AWAC gave wave height measurements every 80 minutes, and SWAN was run using hourly wave spectra. Because of this, the SWAN results were interpolated to the same sampling interval as the AWAC data and the error statistics were calculated using these interpolated values. Figure 11 shows a time series of the significant wave height measured by the AWAC and the simulated significant wave height from SWAN for the duration of the AWAC deployment period. The model achieved a coefficient of determination (R^2) of 0.82, a Root Mean Square Error (RMSE) of 0.32 m and an average percent error of 15.81%. SWAN was run in stationary mode and wind generation was not activated during hindcast trials, which explains much of the differences between the SWAN and AWAC results. However, the goal of the study was

not to replicate conditions as accurately as possible, but instead to ensure that the input conditions used in field site trials were representative of the wave climate at this site.

4.3 Input conditions

Directional wave spectra from a 2005 - 2011 WAVEWATCH III hindcast for the Pacific Northwest were used as offshore input conditions (Garcia-Medina et al., 2013). The WAVEWATCH III hindcast was coupled to a low-resolution SWAN domain extending from Northern California to Washington and covering the entire continental shelf (shown in Appendix D, Figure 1). The local, higher resolution SWAN domain including the NETS and SETS sites was then nested into this coupled system.

Input conditions for the NETS and SETS trials were selected to be representative of the normal range of wave conditions experienced on the Oregon coast. Hourly wave spectra at the offshore boundary of the low-resolution SWAN domain were available from 2005-2011, and these spectra were analyzed based on their probability of occurrence in order to select the appropriate conditions. First, the peak period T_p, significant wave height H_s, and mean wave direction θ were extracted at each point along the offshore boundary of the SWAN domain for each hour in the seven year hindcast. Each parameter was averaged across the offshore boundary to generate a single set of peak parameters (or triplet) for each hour. The triplets were then separated into 120 groups each with the same number of points (and therefore the same probability of occurring) using a 3-dimensional probability density function with 6 frequency bins, 4 wave direction bins, and 5 significant wave height bins. In each group, the centroid of the points was computed, and the hindcast hour with the wave parameters closest to the parameters of the centroid was found. The 120 hours selected using this method were used as the input conditions in the final trials. Two-dimensional histograms showing the bin and centroid locations are shown in Appendix C, Figures 1-3. The T_p, H_s, and θ from the spectra used in the final trials are given in Appendix 2, Table 1.

4.4 Model results

4.4.1 SETS

Plots of the difference in H_s at the SETS site can be seen in Figures 12, from trials with an input peak period T_p of 12.61 s, an input H_s of 5.45 m, and an input θ of -27.11^0. Similar trends were seen in the changes in these parameters when compared to the results of

the parameterized study, including a decrease in the H_s and F_x in the lee of the array and a redirection of waves on either side of the array. The average location of the maximum H_s in the direct lee of the array was determined, and changes in H_s were assessed at this point. A single trial resulted in a percent change in H_s of over 15%. All other trials resulted in a percent change in H_s below 8.5% at this location. The maximum percent decrease in H_s in the parametric study for arrays located 10 km from shore was 6.5%. The percent change in H_s was therefore slightly larger in certain trials at the real sites.

For the NETS and SETS trials, the breaking point was defined as the mean location of maximum dissipation in the direct lee of the array. A total of 34 trials with a closely-spaced array at the SETS site resulted in a change in alongshore force ΔF_y above the threshold value at the breaking point, along with 39 trials with a widely-spaced array. Input conditions that resulted ΔF_y above the threshold value can be seen in Figure 13. No trials from the parametric study reached the threshold ΔF_y when the array was located 10 km from shore.

To assess the importance of specific bathymetric or coastal features in threshold exceedance, the location of the maximum ΔF_y was found for each trial. It was found that the maximum ΔF_y occurred at major coastal features (the Newport jetties and Yaquina Head) in the majority of trials. To determine whether it was exclusively these features resulting in threshold exceedance, the location of the maximum ΔF_y was found excluding the area in the immediate vicinity of Yaquina Head and the Newport jetties. In this case, only two simulations with a widely-spaced array and seven simulations with a closely-spaced array resulted in ΔF_y values over the threshold, indicating that these coastal features were playing a significant role in threshold exceedance. The location of the Newport jetties and Yaquina Head were subsequently removed from the analysis to focus on threshold exceedance on open coastal regions.

Similar to trials from the parameterized study, the SETS trial results show that the threshold value was much more likely to be exceeded in trials with large T_p and H_s values when the two dominant coastal features were removed. All of the nine trials that met the threshold ΔF_y value had an H_s over 5 m. Additionally, only one trial with an input H_s over 5 m in trials with a closely-spaced array did not meet the threshold value, indicating that H_s was an important input factors influencing ΔF_y. All trials that met the threshold ΔF_y value had a T_p of over 12 s.

Although the wave conditions (large H_s and T_p) and array configurations (closely-spaced) that led to significant nearshore impact were consistent with the parameterized study when major coastal features were excluded, the spatial variability of the ΔF_y appeared to be heavily influenced by local bathymetry. Longshore ΔF_y transects can be seen in Figure 14, from trials with an input T_p of 12.61 s, an input H_s of 5.45 m, and an input θ of -27.11. These transects, when compared to the longshore ΔF_y transects from the parameterized study, do not appear to follow the same spatial trends.

4.4.1 NETS

Plots of the difference in significant wave height H_s at the NETS site can be seen in Figures 15, from trials with an input peak period T_p of 12.61 s, an input H_s of 5.45 m, and an input θ of -27.11^0. The maximum percent decrease in H_s was 11.8% for trials at the NETS field site, with 15 trials with a closely-spaced array resulting in a percent decrease over 10%. Additionally, 89.2% of trials (107 out of 120) with a closely-spaced array led to changes in F_y above the threshold. The maximum percent decrease in H_s in the lee of a widely-spaced array was 6.3%. Of the 120 trials with a widely-spaced array, 92 resulted in a significant change in F_y at the location of maximum dissipation. Input conditions that resulted in changes in F_y over the threshold value can be seen in Figure 15.

The location of maximum ΔF_y was found for all NETS trials. Only 11 trials (eight with a closely-spaced array and three with a widely-spaced array) had their maximum ΔF_y at a location other than Yaquina Head, indicating that this feature was an important parameter controlling threshold exceedance.

5. Conclusions

A methodology for modeling WEC arrays in SWAN was developed and applied in the parametric study of the impacts of WEC arrays on nearshore forcing parameters. WEC arrays were incorporated in the SWAN domain through the external modification of the wave spectra at the devices locations. This technique employs an experimentally determined PTF that allows for a realistic representation of energy extraction by WEC devices. A threshold longshore force F_y value was defined to help assess the significance of the changes in nearshore forcing. Nearshore wave-induced forcing terms F_x and F_y were analyzed for each set of input conditions and for each WEC design.

Larger maximum ΔF_y values at the location of maximum dissipation were seen with larger input significant wave heights and larger input peak periods. Wave regeneration in the shadow zone was found to increase with an increase in the distance between the array and the shore and with an increase in directional spreading, implying that the largest differences in the nearshore forcing due to WEC arrays will occur in high energy swell seas with a WEC array located close to shore. Closely-spaced arrays had a much larger impact on wave height and direction in the direct lee of the array, but the differences between cases due to WEC spacing decreased with increasing distance from the array.

The results from the parametric trials were compared to the results of trials conducted at two permitted NNMREC test sites to assess the validity of the conclusions made in this parametric study when applied to sites with more realistic bathymetries. In this study, it was found that similar wave conditions and array configurations resulted in changes in F_y over the established threshold value. However, the spatial variability of the changes in F_y appeared to be heavily influenced by the local bathymetry.

Acknowledgements

This material is based upon work supported by the Department of Energy under Award Number DE-FG36-08GO18179. This report was prepared as an account of work sponsored by an agency of the United States Government. Neither the United States Government nor any agency thereof, nor any of their employees, makes any warranty, expressed or implied, or assumes any legal liability or responsibility for the accuracy, completeness, or usefulness of any information, apparatus, product, or process disclosed, or represents that is use would not infringe privately owned rights. Reference herein to any specific commercial product, process, or service by trade name, trademark, manufacturer, or otherwise does not necessarily constitute or imply its endorsement, recommendation, or favoring by the United States Government or any agency thereof. Their views and opinions of the authors expressed herein do not necessarily state or reflect those of the United States Government or any agency thereof. The authors would like to thank Gabriel Garcia-Medina for providing the Pacific Northwest hindcast data used as input conditions in the real test sites, as well as Ed Dever, Craig Risien, and the Ocean Observatories Initiative for providing the AWAC data used in model validation.

Figures

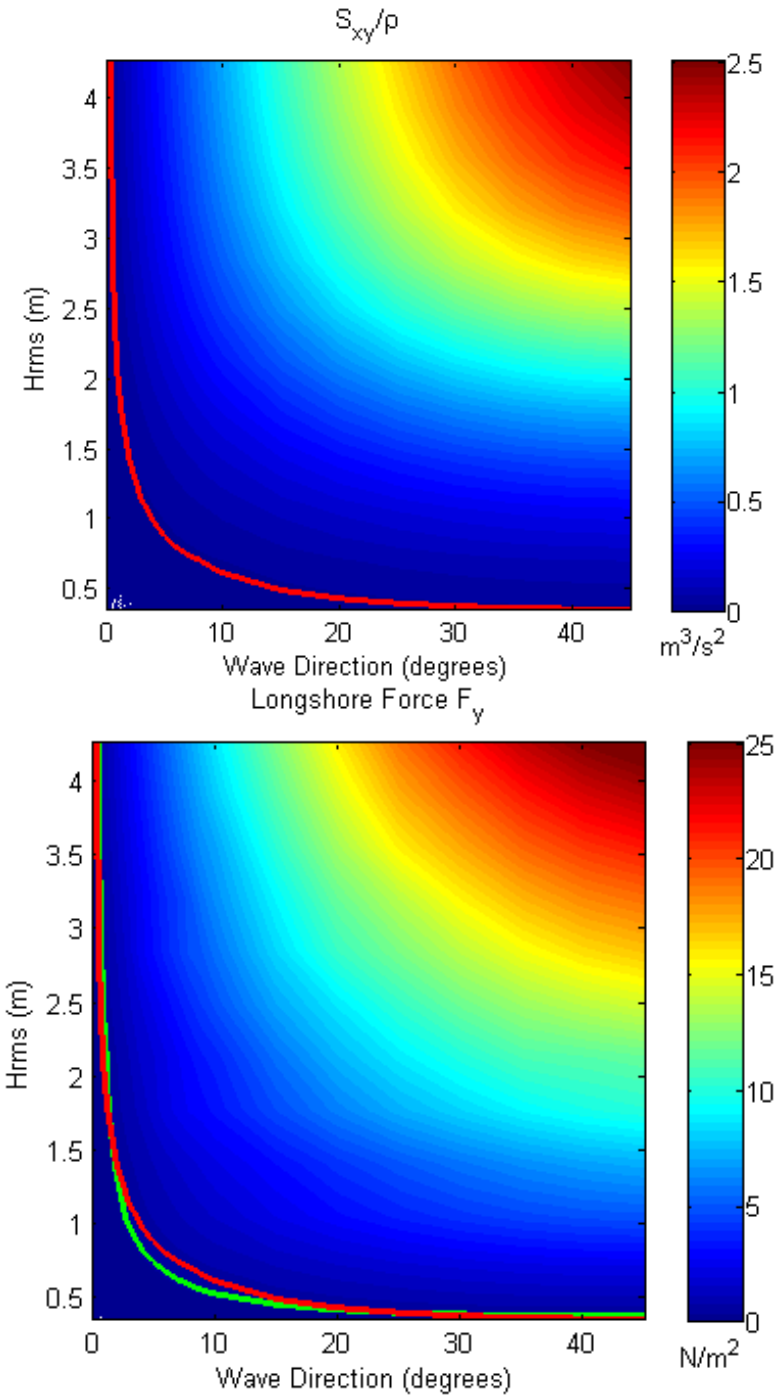

Figure 1. a) S_{xy}/ρ at the 6.5 m contour line and **b)** the F_y at the location of maximum dissipation as a function of H_{rms} and θ. The S_{xy}/ρ = 0.0314 m^3/s^2 contour line is shown in red, along with the F_y = 0.44 N/m^2 contour line in green.

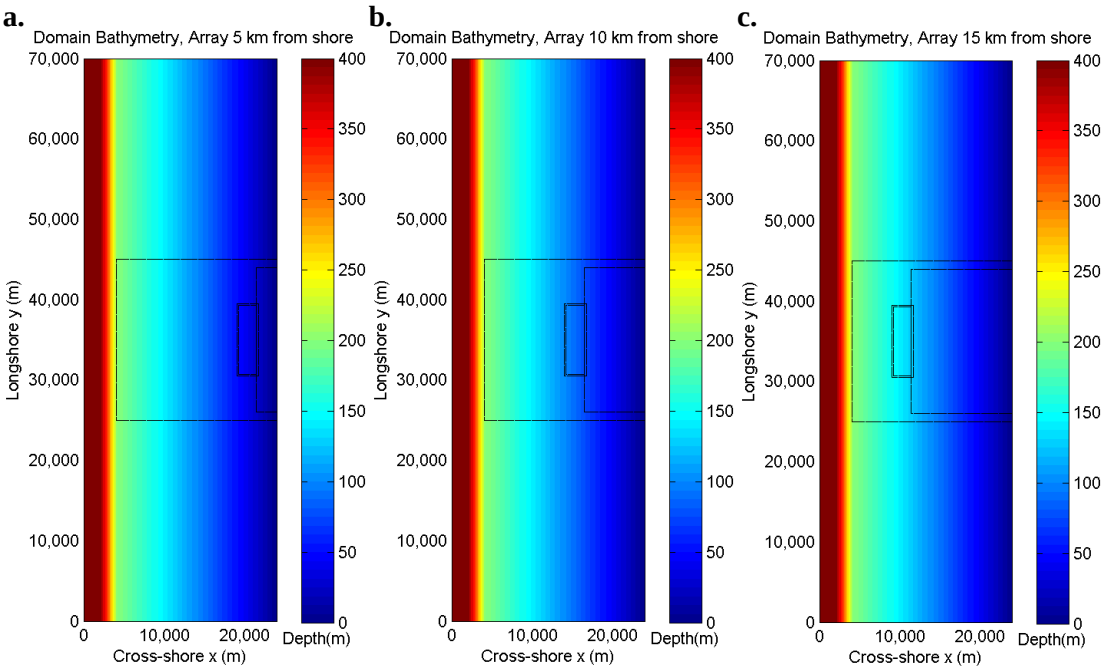

Figure 2. Model bathymetry for cases with an array located **a)** 5 km from shore, **b)** 10 km from shore, and **c)** 15 km from shore. Black lines indicate a nested grid with a different spatial resolution.

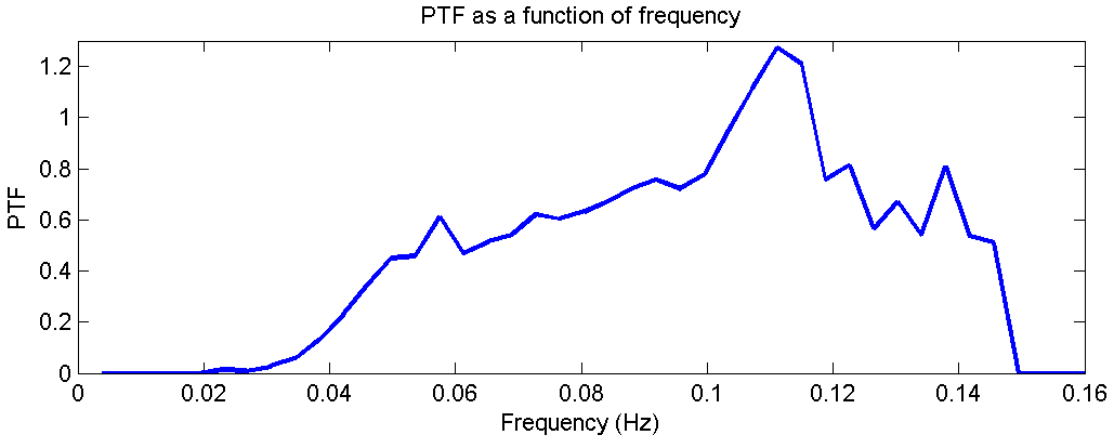

Figure 3. The experimentally determined PTF as a function of wave frequency (Rhinefrank et al., 2013).

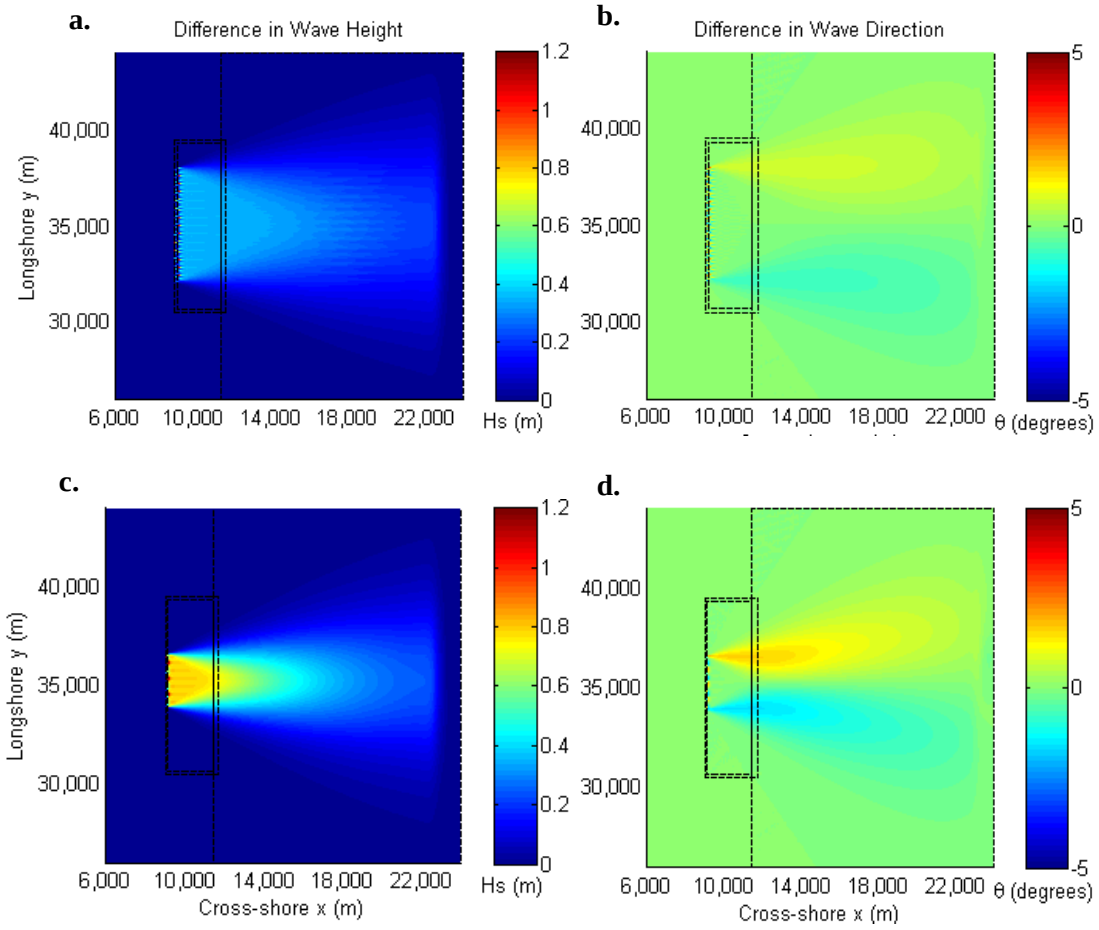

Figure 4. Differences in **a)** H_s (left) in the lee of a widely-spaced array, **b)** θ in the lee of a widely-spaced array, **c)** H_s (left) in the lee of a closely-spaced array, and **d)** θ in the lee of a closely-spaced array from trials with an input H_s = 6 m, an input T_p = 12 s, low directional spread (14^0), and an array located 15 km from shore. The dotted lines show the located of nested grids.

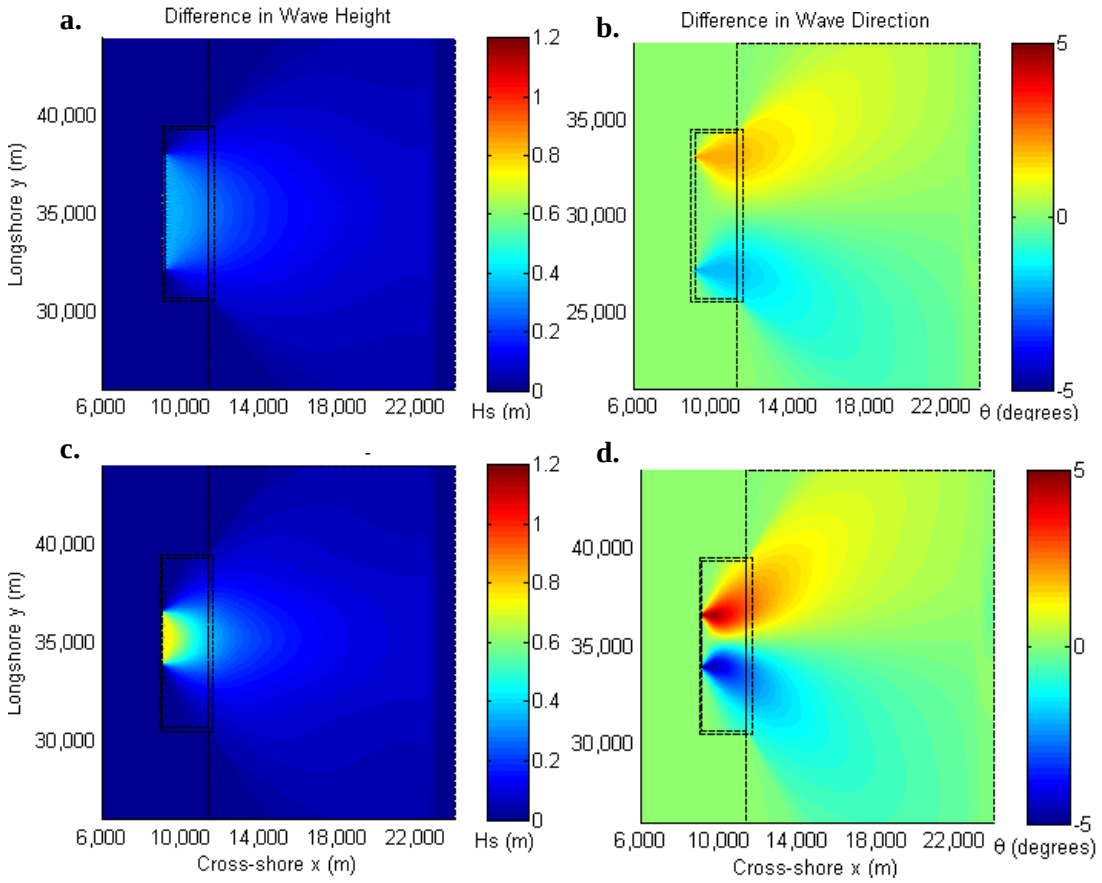

Figure 5. Differences in **a)** H_s (left) in the lee of a widely-spaced array, **b)** θ in the lee of a widely-spaced array, **c)** H_s (left) in the lee of a closely-spaced array, and **d)** θ in the lee of a closely-spaced array from trials with an input H_s = 6 m, an input T_p = 12 s, high directional spread (35^0), and an array located 15 km from shore. The dotted lines show the located of nested grids.

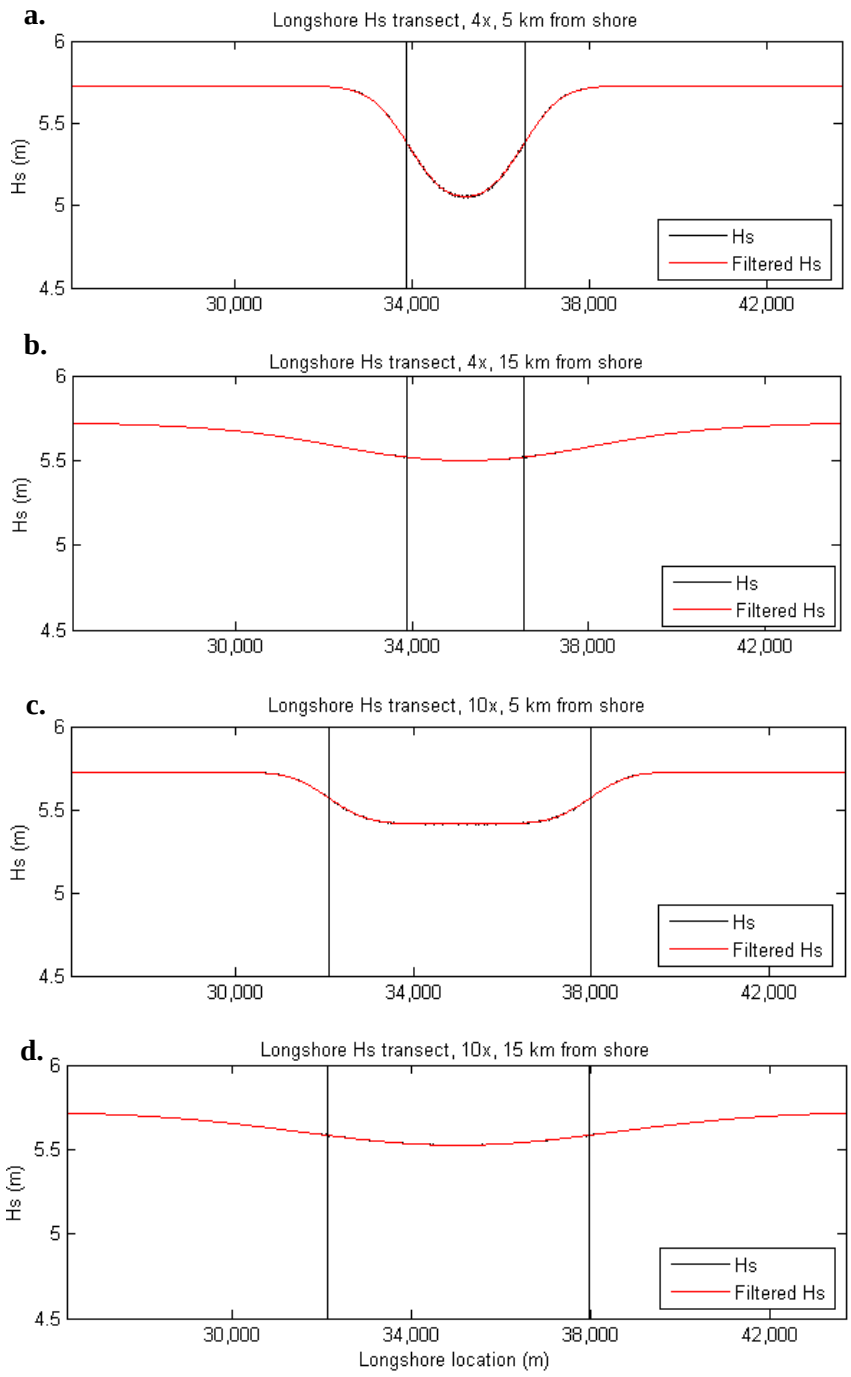

Figure 6. Longshore H_s transects in the lee of a closely-spaced array located **a)** 5 km and **b)** 15 km offshore, as well as a widely-spaced array located **c)** 5 km and **d)** 15 km offshore with an input H_s = 6 m, an input T_p = 12 s, and low directional spread (14^0). The transect was taken from the location of the maximum H_s in the absence of an array. The vertical black lines show the longshore location of the edges of the WEC array.

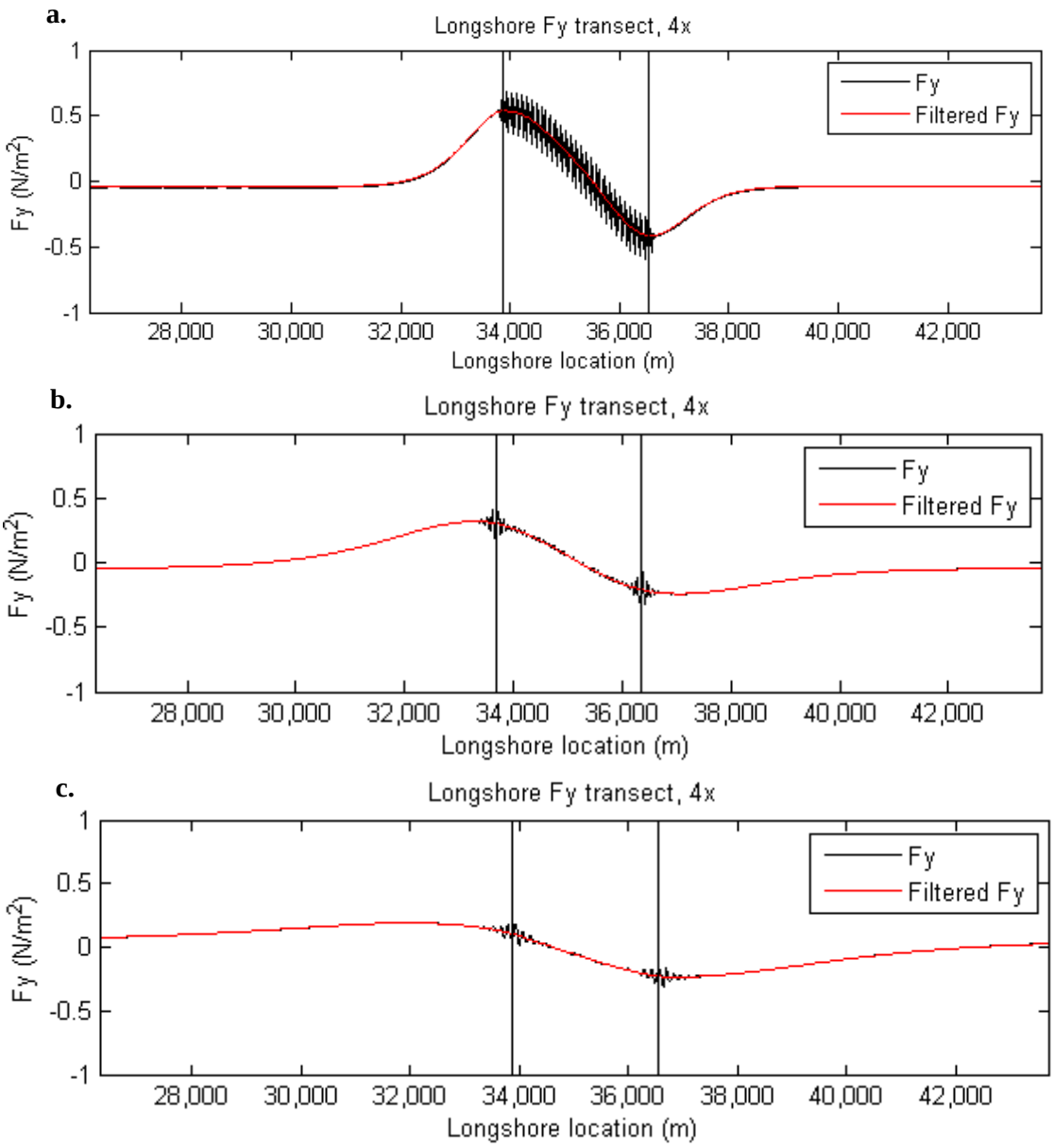

Figure 7. Longshore F_y transects in the lee of a closely-spaced array located **a)** 5 km, **b)** 10 km, and **c)** 15 km from shore with an input H_s = 6 m, an input T_p = 12 s, and low directional spread (14°). The transect was taken from the location of maximum dissipation. The vertical black lines show the longshore location of the edges of the WEC array.

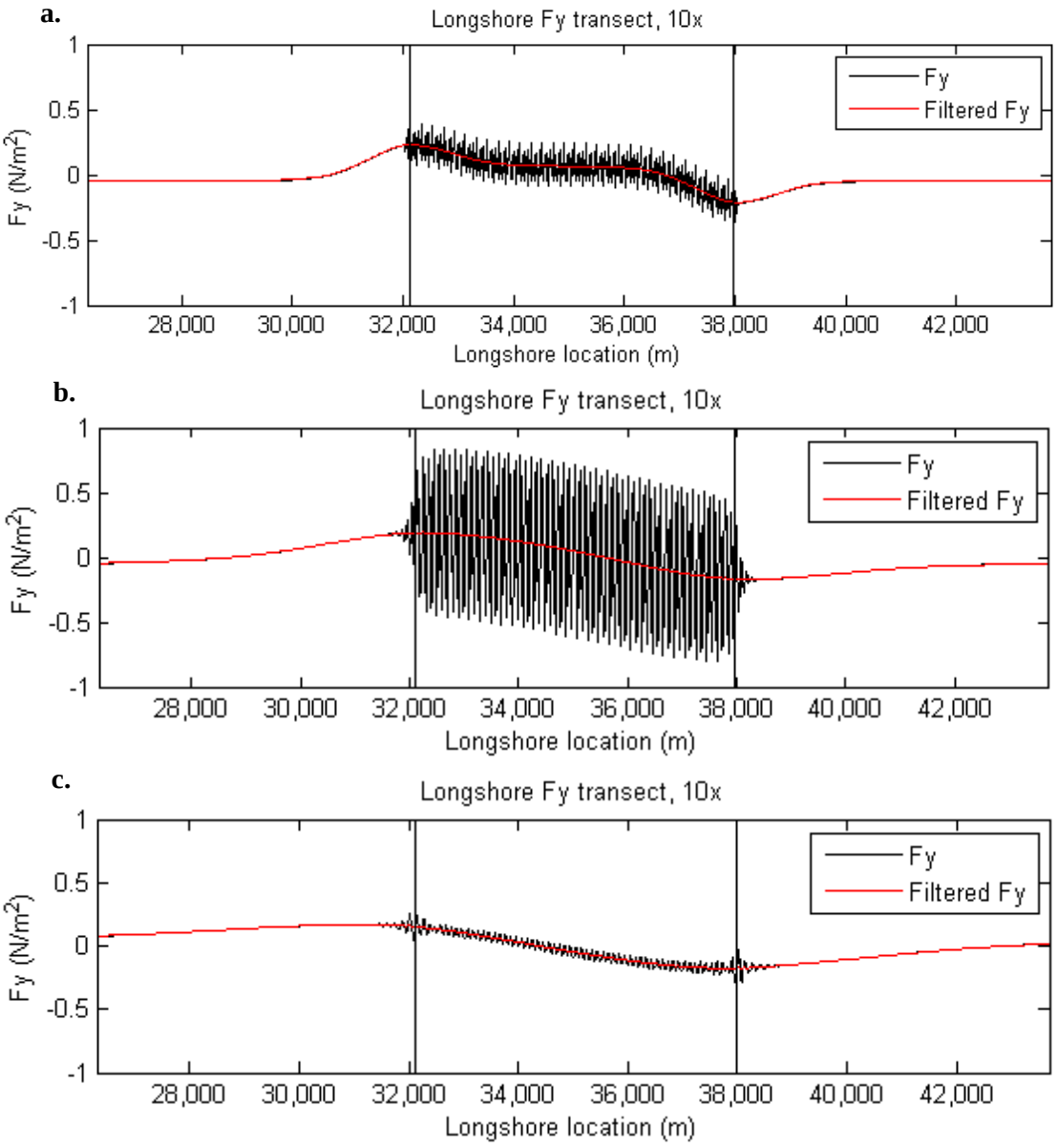

Figure 8. Longshore F_y transects in the lee of a widely-spaced array located **a)** 5 km, **b)** 10 km, and **c)** 15 km from shore with an input H_s = 6 m, an input T_p = 12 s, and low directional spread (14°). The transect was taken from the location of maximum dissipation. The vertical black lines show the longshore location of the edges of the WEC array.

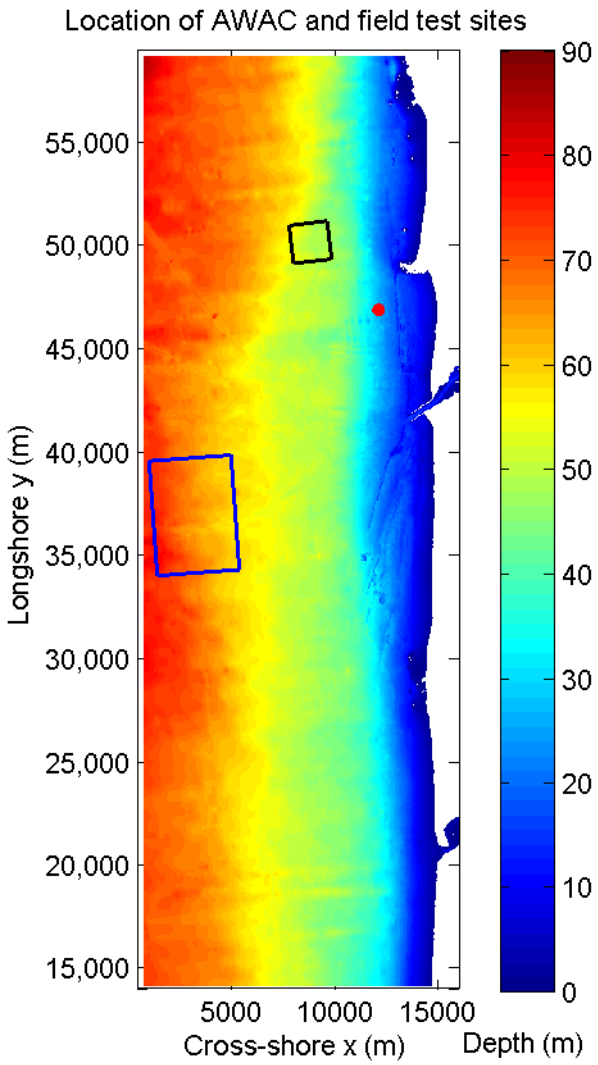

Figure 9. Location of the NETS site (in black), the SETS site (in blue), and the AWAC used in model validation (in red).

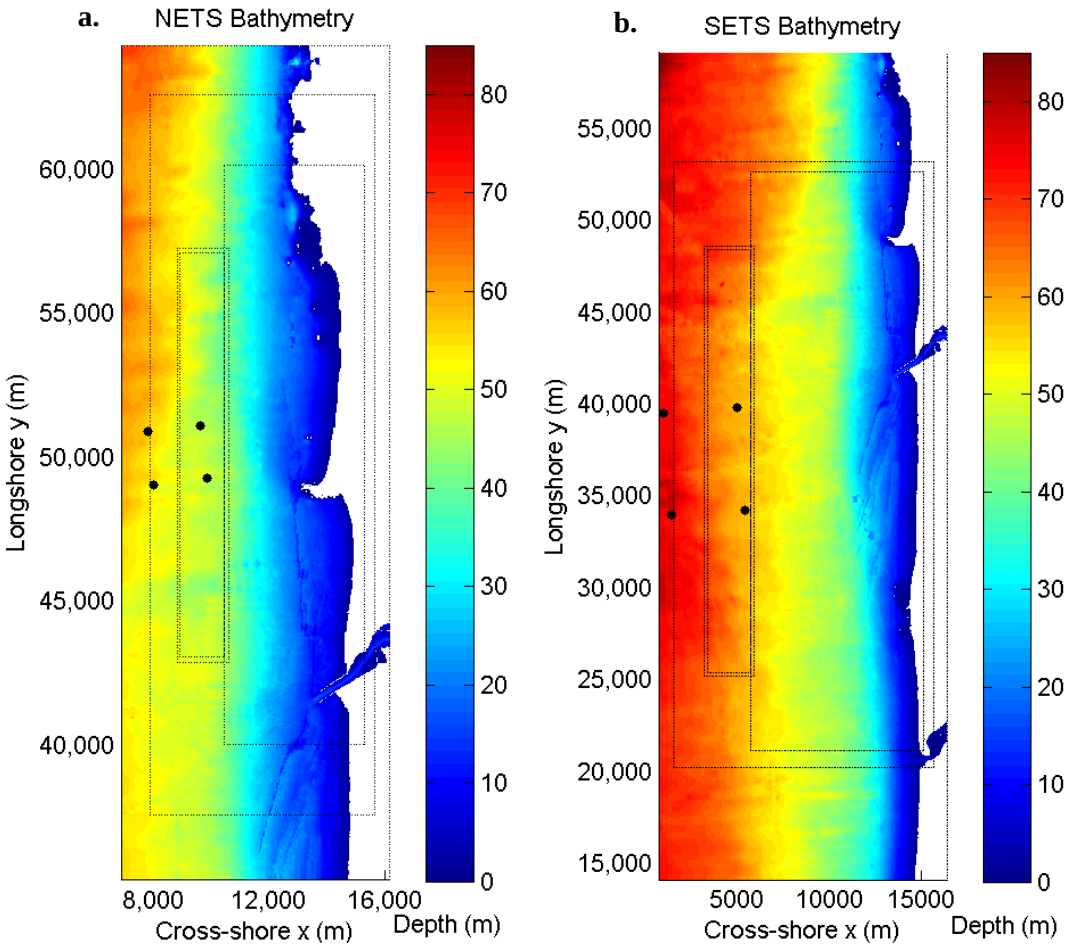

Figure 10. Model bathymetry for simulations at **a)** the NETS site and **b**) the SETS site. Black lines indicate a nested grid with a different spatial resolution.

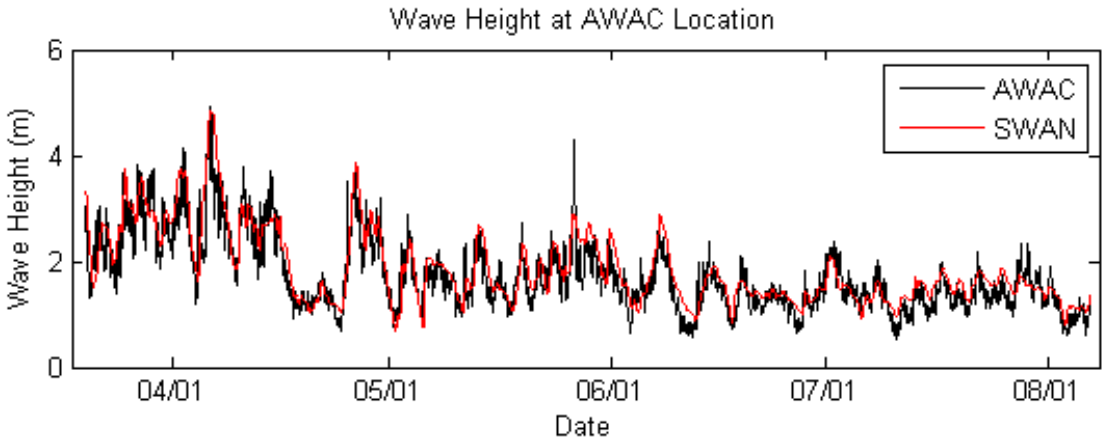

Figure 11. Significant wave height from the processed AWAC data (black) and the SWAN trials (red) for the duration of the AWAC deployment period (March to August 2011).

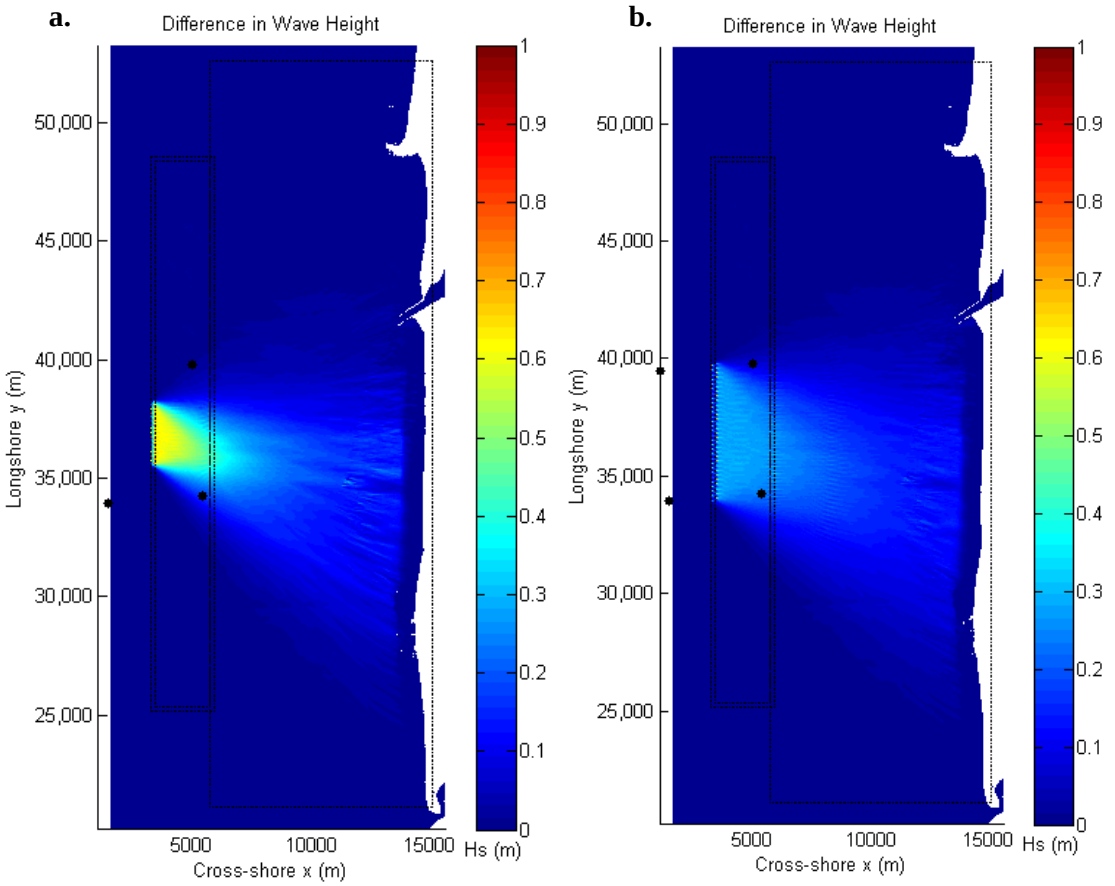

Figure 12. Difference in significant wave height in the lee of **a)** a closely-spaced array and **b)** a widely-spaced array at the SETS site for trials with an input H_s = 5.45 m, an input T_p = 12.61 s, and an input θ = -27.11^0.

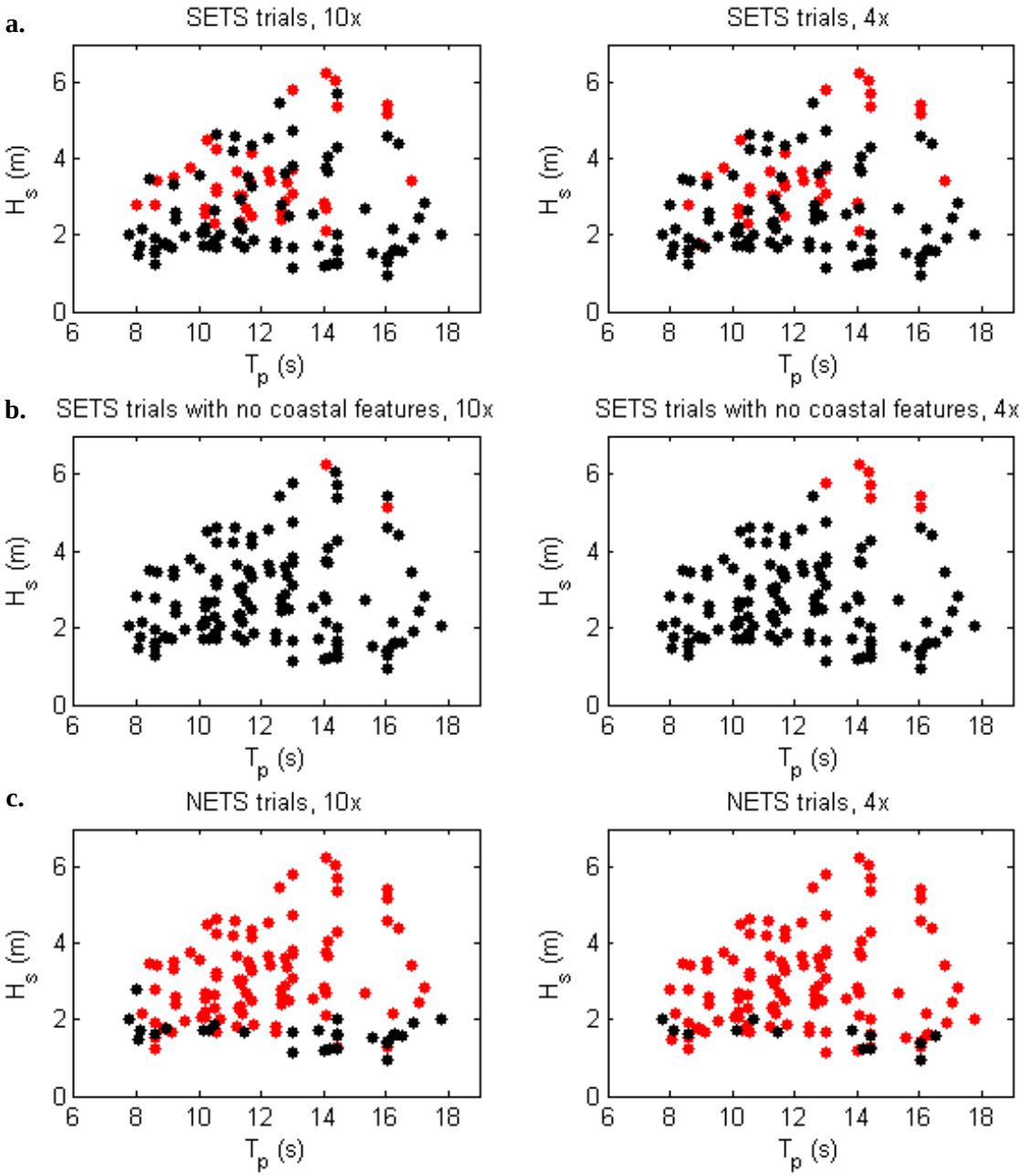

Figure 13. Input H_s and T_p from **a)** all trials at the SETS site, **b)** all trials at the SETS site when the location of the jetties and Yaquina Head have been excluded from the analysis, and **c)** all trials from the NETS sites. Figures on the right are from trials with a closely-spaced and figures on the left are from trials with a widely-spaced array. Trials that met the threshold ΔF_y value are shown in red.

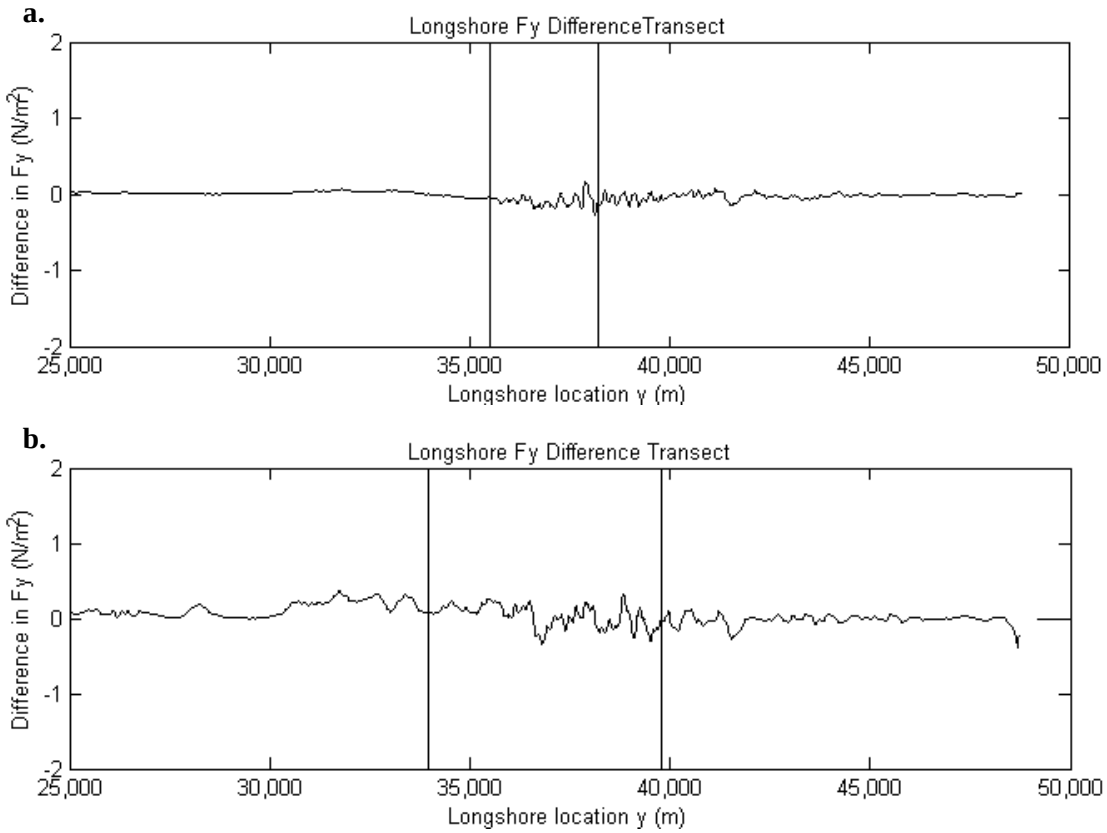

Figure 14. Longshore F_y transects in the lee of **a)** a closely-spaced array and **b)** a widely-spaced array (bottom) at the SETS site for trials with an input H_s = 5.45 m, an input T_p = 12.61 s, and an input θ = -27.11^0.

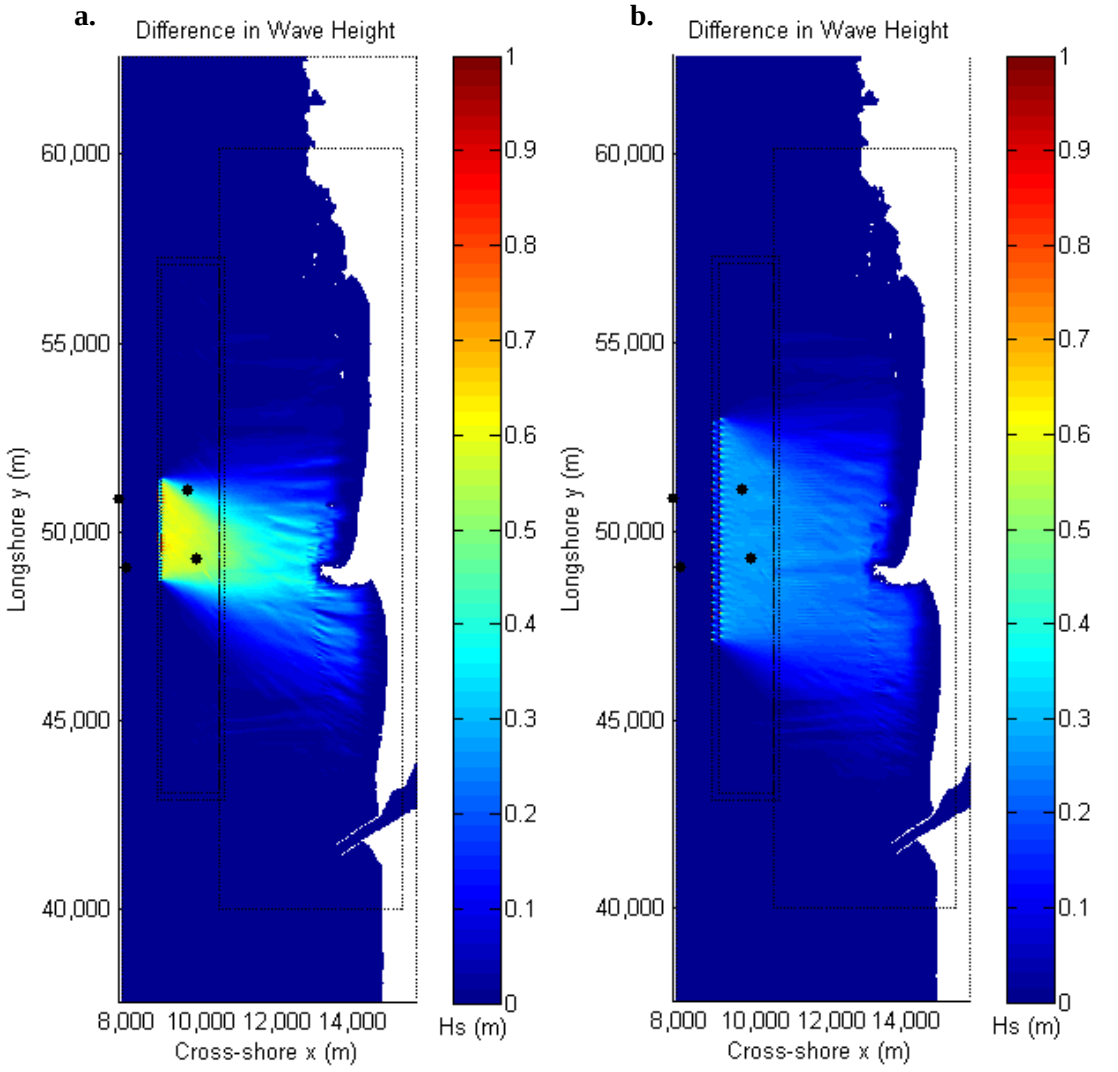

Figure 15. Difference in significant wave height in the lee of **a)** a closely-spaced array and **b)** a widely-spaced array at the NETS site for trials with an input H_s = 5.45 m, an input T_p = 12.61 s, and an input θ = -27.11^0.

Tables

Table 1. Input conditions for all trials in the parametric study. Each set of conditions was simulated with a closely-spaced array, a widely-spaced array, and no array, with arrays located 5, 10, and 15 km from shore.

Hs (m)	Tp (s)	Directional Spread (°)
2	6	14, 35
6	6	14, 35
2	7	14, 35
6	7	14, 35
2	8	14, 35
6	8	14, 35
2	9	14, 35
6	9	14, 35
2	10	14, 35
6	10	14, 35
2	12	14, 35
6	12	14, 35
2	14	14, 35
6	14	14, 35
2	16	14, 35
6	16	14, 35
2	18	14, 35
6	18	14, 35

Table 2. Results from trials with an array located 5 km from shore. Trials that generated a longshore force above the established threshold value are marked with an X.

	Low Directional Spread									
	Hs (m)	Peak Period Tp (s)								
		6	7	8	9	10	12	14	16	18
4x spacing	6			x	x	x	x	x	x	x
	2									
10x spacing	6									
	2									
High Directional Spread										
4x spacing	6				x		x	x	x	x
	2									
10x spacing	6									
	2									

References

Abanades, J.; Greaves, D.; and Iglesias, G. 2014a, "Wave farm impact on the beach profile: A case study." Coast. Eng. 86, pp. 36-44.

Abanades, J.; Greaves, D.; and Iglesias, G. 2014b, "Coastal defence through wave farms." Coast. Eng. 91, pp 299-307.

Booij, N.; Ris, R.C.; Holthuijsen, L.H. 1999, "A third-generation wave model for coastal regions: 1. Model description and validation." J. Geophys. Res. Oceans 104 (C4), pp. 7649-7666.

Bowen, A.J. 1969, "Rip Currents 1. Theoretical Investigations." J. Geophys. Res. 74 (23), pp. 5467-5478.

Carballo, R. and Iglesias, G., 2013. "Wave farm impact based on realistic wave-WEC interactions," Energy 51, pp. 216-219.

Carignan, K.S.; Taylor, L.A.; Eakins, B.W.; Warnken, R.R.; Lim, E.; and Medley, P.R. 2009, "Digital Elevation Model of Central Oregon Coast: Procedures, Data Sources and Analysis," NOAA Technical Memorandum NESDIS NGDC-25, U.S. Dept. of Commerce, Boulder, CO, 38 pp.

Dean, R.G. and Dalrymple, R.A. 2010, Water Wave Mechanics for Engineers and Scientists. World Scientific Publishing Co. Pte. Ltd., Singapore, Chap. 4.

Feddersen, F; Guza, R.T.; Elgar, S.; and Herbers, T.H.C. 1998, "Alongshore momentum balances in the nearshore," J. Geophys. Res. 103 (C8), pp. 15667-15676.

Garcia-Medina, G.; Ozkan-Haller, H.T.; Ruggiero, P.; and Oskamp, J. 2013, "An inner-shelf wave forecasting system for the US Pacific Northwest," Weather Forecast. 28, pp. 681-703.

Gonzalez-Santamaria, R.; Zou, Q.P.; and Pan, S. 2013, "Impacts of a wave farm on waves, currents and coastal morphology in South West England," Estuar. Coasts 1, pp. 1-14.

Guza, R.T.; Thorton, E.B.; and Christensen Jr, N. 1986, "Observations of Steady Longshore Currents in the Surf Zone." J. Phys. Oceanogr. 16, pp. 1959-1969.

Holthuijsen, L.H.; Herman, A.; and Booij, N. 2003, "Phase-decoupled refraction-diffraction for spectral wave models." Coast. Eng. 49, pp. 291-305.

Lenee-Bluhm, P.; Paasch, R.; and Ozkan-Haller, H.T. 2011. "Characterizing the wave energy resource of the US Pacific Northwest." Renew. Energ. 36, pp. 2106-2119.

Longuet-Higgins, M.S. and Stewart, R.W. (1964) Radiation stresses in water waves; a physical discussion, with applications. Deep-Sea Research 11: 529-562.

Mendoza, E.; Silva, R.; Zanuttigh, B.; Angelilli, E.; Andersen, T.L.; Marinelli, L.; Norgaard, J.Q.H.; and Ruol, P. 2013, "Beach response to wave energy converter farms acting as coastal defence." Coast. Eng. 87, pp 97-111

Millar, D.L.; Smith, H.C.M; and Reeve, D.E. 2007, "Modelling analysis of the sensitivity of shoreline change to a wave farm," Oc. Eng. 34, pp. 884-901.

Palha, A.; Mendes, L.; Fortes, C.J.; Brito-Melo, A.; and Sarmento, A. 2010, "The impact of wave energy farms in the shoreline wave climate: Portuguese pilot zone case study using Pelamis energy wave devices." Renew. Energ. 35, pp. 62-77.

Rhinefrank, K., M. Haller, T. Ozkan-Haller, A. Porter, C. McNatt, P. Lenee-Bluhm, and Schumacher, E. 2013, Benchmark Modeling of the Near-Field and Far-Field Wave Effects of Wave Energy Arrays, Columbia Power Technologies Final Report, DE-EE0002658, U.S. Dept. of Energy, www.osti.gov/servlets/purl/1060889/.

Rusu, E. and Soares, C.G. 2013, "Coastal impact induced by a Pelamis wave farm operating in the Portuguese nearshore," Renew. Energ. 58, pp. 34-49.

Smith, H.C.M.; Pearce, C.; and Millar, D.L, 2012. "Further analysis of change in nearshore wave climate due to an offshore wave farm: An enhanced case study for the Wave Hub site." Renew. Energ. 40, pp. 51-64.

Svendsen, I.A, 2006, Introduction to Nearshore Hydrodynamics, World Scientific Publishing Co. Pte. Ltd., Singapore, Chap. 11,12.

SWAN team. 2006a, "SWAN Technical Documentation." Delft University of Technology.

SWAN team. 2006b, "SWAN User Manual." Delft University of Technology.

Vardaro, M.; Risien, C.; Wingard, C.; and Fram, J. 2011, In-Shore Mooring Test 2 (ISMT2) Science Data Report, Oregon State University, Coastal and Global Scale Nodes, Ocean Observatories Initiative.

A Note on the Effect of Asymmetric Directional Spreading on the Total Radiation Stress

Annika O'Dea

Merrick C. Haller

Journal: *American Society of Civil Engineers*
Journal of Waterway, Ports, Coastal and Ocean Engineering

ASCE Journal Services
1801 Alexander Bell Drive
Reston, VA 20191-4400

To be submitted fall 2014

Abstract

The process of wave refraction in nearshore zones results in an asymmetric directional distribution of spectral energy when oblique, multi-directional wave fields propagate into shallow water areas with limited alongshore variability. Here we analyze the effect of this directional asymmetry on wave radiation stress calculations. Net radiation stresses are calculated for a JONSWAP frequency spectrum with both symmetric and asymmetric directional distributions and then compared to those calculated from the commonly-used monochromatic formulation (appropriate for narrow-banded spectrum, symmetric distribution). Past studies have demonstrated that the use of the monochromatic approximation in radiation stress calculations results in a significant overestimation of the radiation stress components S_{xx} and S_{xy} in broad-banded seas. The present results show that the inclusion of directional asymmetry in radiation stress calculations reduces the difference between the full spectral S_{xx} and the monochromatic approximation but increases the difference between the full spectral S_{xy} and the monochromatic approximation for a range of dominant wave directions. The use of a monochromatic approximation of S_{xy} can therefore lead to an overestimation of the actual radiation stress in certain sea states and consequently an overestimation of associated parameters such as alongshore current velocities and alongshore sediment transport rates.

1. Introduction

Radiation stresses, defined as the excess flow of momentum due to the presence of waves (Longuet-Higgins, 1964), are the main drivers behind the cross-shore and longshore forcing that results in wave setup, set-down, and longshore currents (e.g. Svendsen, 2006). Longshore currents entrain and transport sediment and therefore play an important role in short- and long-term coastal evolution (Komar, 1998). For a real wave field, with the total energy being a linear combination of a number of components distributed in frequency and direction, the off-diagonal radiation stress component S_{xy} is defined by:

$$S_{xy} = \rho g \int_0^{\infty} \int_{-\pi}^{\pi} E(f,\theta) \frac{c_g(f)}{c(f)} \sin(\theta)\cos(\theta) d\theta df \tag{1}$$

where ρ is the density of seawater, g is the acceleration of gravity, $c_g(f)$ is the frequency-dependent group velocity, $c(f)$ is the frequency-depend phase velocity, θ is the wave angle of approach, and $E(f,\theta)$ is the frequency-directional energy spectrum (in units of m^2s/radian) (Battjes, 1972). Equation (1) requires knowledge of the full frequency and directional distribution of spectral energy, which is not always available in practice. For this reason, the monochromatic radiation stress formulation is typically used as an approximation using the total energy and parameter values at the peak frequency and dominant wave direction, with the assumption that the spectrum is narrow-banded in frequency and directional space and therefore the difference between the monochromatic formulation and the true formulation is minimal. The monochromatic S_{xy} formulation reduces to:

$$S_{xy} = \frac{1}{8} \rho g H^2 \frac{c_g}{c} \sin(\theta)\cos(\theta) \tag{2}$$

where H is the wave height, c_g is the group velocity, c is the phase velocity, and θ is the wave angle of approach (Longuet-Higgins, 1970).

The accuracy of this narrow-banded (i.e. monochromatic) radiation stress approximation has been the focus of a number of studies since the radiation stress formulation was first proposed. Battjes (1972) conducted an analytic analysis of the ratio of total energy to the radiation stress using the common Pierson-Moskowitz (PM) frequency spectrum and

several symmetric directional spreading functions. He determined that the spreading of energy over a range of frequencies did not significantly affect the ratio of energy to radiation stress, but that high directional spreading (or short-crestedness) did have an effect on this ratio. That study found that the use of the narrow-banded approximation for the S_{xx} and S_{xy} components in short-crested seas significantly overestimated the actual radiation stress.

In a more recent study, Feddersen (2004) followed the analytic method used by Battjes (1972) to compare the narrow-banded and true S_{xx} and S_{xy} radiation stress components using a range of directional spreads, and then compared these values to those observed in the field at 8 m water depth on the Outer Banks, NC, where broad-banded sea states are common. Similar to the method employed by Battjes (1972), this treatment included a PM frequency spectrum along with a symmetric directional spreading function. This study confirmed that the narrow-banded S_{xx} and S_{xy} radiation stress components were systematically larger than the true radiation stress values calculated from the full frequency-directional spectrum, and quantified the dependence of this difference on the directional spread.

The studies mentioned above demonstrated that the use of the narrow-banded radiation stress approximations can result in biased radiation stress values and consequently biased longshore current and sediment transport values. However, a recent study by Lee et al. (2010) indicated that the symmetric directional spreading function is less appropriate in shallow water, where radiation stress forcing is most important. Those authors demonstrated that wave refraction in shallow water results in an asymmetric directional distribution of spectral energy, and proposed a modification to a commonly-used directional spreading function to account for this asymmetry. Here, we investigate the impact of an asymmetric directional distribution on the true radiation stress values.

The main objective of this study is to analyze the effect of asymmetry in the directional distribution of spectral energy on calculations of wave-induced radiation stresses. The wave-induced radiation stresses are determined using a) a narrow-banded approximation (i.e. monochromatic waves), b) a JONSWAP frequency spectrum with a symmetric directional spreading function, and c) a JONSWAP frequency spectrum with an asymmetric directional spreading function, and the resulting values are compared. Basic conclusions about the importance of directional asymmetry in nearshore radiation stress calculations are made, and the implications of the use of narrow-banded approximations or symmetric spectra in the calculation of radiation stress for coastal engineering projects are discussed.

2. Methods

2.1 Directional spreading function

2.1.1 Symmetric spectrum

For the symmetric directional spectrum, the Longuet-Higgins et al. (1961) formulation for the directional spreading function was used, where the directional spreading function $G(f,\theta)$ can be written as

$$G(f,\theta) = G_O \cos^{2s}\left(\frac{\theta-\theta_p}{2}\right) \tag{3}$$

where

$$G_O = \left[\int_{\theta_{\min}}^{\theta_{\max}} \cos^{2s}\left(\frac{\theta-\theta_p}{2}\right)\right]^{-1} \tag{4}$$

$$s = \begin{cases} s_{\max}\cdot(f/f_p)^5, & f \le f_p \\ s_{\max}\cdot(f/f_p)^{-2.5}, & f \ge f_p \end{cases} \tag{5}$$

where θ_p is the dominant direction, $\theta_{\min}$ and $\theta_{\max}$ are the maximum and minimum angle of interest (π and $-\pi$), and f_p is the peak frequency. The spreading parameter s was developed by Goda and Suzuki (1975).

2.1.2 Asymmetric spectrum

As multi-directional wave fields propagate in intermediate to shallow water depths, each directional component will refract at a different rate, resulting in an asymmetric distribution of spectral energy around the dominant wave direction. A model function for this asymmetric distribution was given by Lee et al. (2010). In the asymmetric case, the spreading function $G_A(f,\theta)$ is given by:

$$G_A(f,\theta) = G_{OA} \cos^{2s}\left(\frac{\theta-\theta_p}{2}\xi\right) \tag{6}$$

$$G_{OA} = \left[\int_{\theta_{\min}}^{\theta_{\max}} \cos^{2s}\left(\frac{\theta - \theta_p}{2} \xi \right) \right]^{-1} \tag{7}$$

$$\xi = \begin{cases} \exp(-\mu), \theta \geq \theta_p \\ \exp(\mu), \theta \leq \theta_p \end{cases} \tag{8}$$

where μ is the asymmetry parameter and s as given in Equation 5. When μ is 0 (as would be the case if the dominant wave direction were shore normal), ξ is equal to 1 and the asymmetric directional spreading function defined above collapses into the symmetric directional spreading function proposed by Longuet-Higgins et al. (1961). For a set of incident deep water conditions, Lee et al. found μ and s_{max} as a function of relative depth h/L_{po}, where h is the water depth and L_{po} is the offshore peak wavelength. To determine μ and s_{max}, Lee et al. (2010) decomposed the wave spectrum into frequency and directional components in deep water, and then shoaled and refracted each component across a nearshore domain. The authors then found the directional spreading function that best fit this nearshore wave spectrum. The directional spreading functions were then compared to field data from Duck, NC to validate their proposed directional spreading formulation. The μ and s_{max} values proposed by Lee et al. for different input conditions were used in all calculations. Both a high directional spread case (s_{max} = 10) and a low directional spread case (s_{max} = 75) were considered. The offshore s_{max} and θ values along with the μ and s_{max} values at the 10 m contour line are listed in Table 1. The directional limits $\theta_{\min}$ and $\theta_{\max}$ were then given by the following equations:

$$\theta_{\min} = \theta_p - \frac{2\pi}{1+\exp(2\mu)}, \quad \theta_{\max} = \theta_p + \frac{2\pi}{1+\exp(-2\mu)} \tag{9}$$

For further discussion of the asymmetric directional spread function, see Lee et al. (2010).

2.2 Frequency spectrum

The frequency-directional wave spectrum $E(f,\theta)$ is a product of the frequency spectrum $S(f)$ and the directional spreading function $G(f,\theta)$ as shown in Equation 10:

$$E(f,\theta) = S(f)G(f,\theta) \tag{10}$$

where $E(f,\theta)$ is in units of m^2s/rad. For the JONSWAP spectrum (Hasselmann et al, 1973; Goda 2000), $S(f)$ is given by:

$$S(f) = \beta_J H_s^2 T_P^{-4} f^{-5} \exp[-1.25(T_P f)^{-4}]\gamma^{\exp[-(T_P f-1)^2/2\sigma^2]} \tag{11}$$

where f is the frequency, H_s is the significant wave height, T_p is the peak period, γ is the peak enhancement parameter, and with

$$B_J \cong \frac{0.0624}{0.23+0.0336\gamma-0.185(1.9+\gamma)^{-1}}[1.094-0.01915\ln\gamma] \tag{12}$$

$$\sigma = \begin{cases} \sigma_a = 0.07 : f \le f_p \\ \sigma_b = 0.09 : f \ge f_p \end{cases} \tag{13}$$

$$T_P \cong T_s[1-0.132(\gamma+0.2)^{-0.559}] \tag{14}$$

where T_s is the significant period. A peak enhancement parameter value of $\gamma = 3.3$ was used in all trials, and the spectra were calculated at the 10 m contour line.

2.3 Input conditions

An offshore significant wave height H_{so} of 5 m and a significant period T_{so} of 10s were used in all calculations along with three offshore wave angles ($\theta_o = 0^0$, 30^0, and 60^0) and two directional spreads (offshore s_{max} = 10 and 75). All calculations were conducted at the 10 m contour line. The significant wave height H_s and dominant wave direction θ_p at the 10 m contour were calculated from the offshore conditions using linear shoaling and Snell's Law. Input conditions were chosen to match those in the Lee et al. (2010), and the spreading parameter s_{max} and asymmetry parameter μ suggested by Lee et al. for each set of conditions

were used in the directional spreading function calculations (Lee et al. (2010), see Figures 5 and 6, respectively). Input conditions for all trials are given in Table 1.

2.4 Radiation stress

The radiation stress tensor S_{ij} was then numerically determined using a) a narrow-banded approximation (i.e. monochromatic waves), and the full frequency-directional spectrum for b) a symmetric directional distribution, and c) an asymmetric directional distribution. The radiation stress formulations for narrow-banded (nb) seas can be rewritten in the form shown in Equations 16-18 (Svendsen, 2006):

$$S_{xx} = \frac{1}{8}\rho g {H_{rms}}^2 [n(\cos^2\theta + 1) - \frac{1}{2}] \tag{16}$$

$$S_{yy} = \frac{1}{8}\rho g {H_{rms}}^2 [n(\sin^2\theta + 1) - \frac{1}{2}] \tag{17}$$

$$S_{xy} = S_{yx} = \frac{1}{16}\rho g {H_{rms}}^2 n \sin 2\theta \tag{18}$$

where H_{rms} is the root mean squared wave height, θ is the wave direction, k is the wave number, and h is the water depth, and with n given by Equation 19.

$$n = \frac{1}{2}\left(1 + \frac{2kh}{\sinh(2kh)}\right) \tag{19}$$

If the full frequency-directional spectrum is known, the radiation stress can be calculated from the extended equations given by Equations 20-22:

$$S_{xx} = \rho g \int_0^\infty \int_{\theta_{\min}}^{\theta_{\max}} E(f,\theta)[n(f)(\cos^2\theta + 1) - \frac{1}{2}] d\theta df \tag{20}$$

$$S_{yy} = \rho g \int_0^\infty \int_{\theta_{\min}}^{\theta_{\max}} E(f,\theta)[n(f)(\sin^2\theta + 1) - \frac{1}{2}] d\theta df \tag{21}$$

$$S_{xy} = S_{yx} = \rho g \int_0^\infty \int_{\theta_{\min}}^{\theta_{\max}} \frac{1}{2} E(f,\theta) n(f)(\sin 2\theta) d\theta df \tag{22}$$

where n is now a function of frequency. These equations, in addition to Equations 16-18, were used to calculate the total radiation stress value at the 10 m contour line.

3. Results and Discussion

An example of the asymmetry resulting from the inclusion of the asymmetric directional spreading function formulation is shown in Figure 1a) and 1b), which includes both the symmetric and the asymmetric directional spreading function at the peak frequency as a function of wave direction for cases with an offshore s_{max} = 10 and $\theta_{po} = 30^0$ and 60^0, respectively. The use of an asymmetric directional spreading function results in a visibly asymmetric wave spectrum, shown in Figure 2.

The wave-induced radiation stresses were calculated using the three previously described methods, and the resulting values for the narrow-banded formulation are shown in Tables 2. Figure 3 shows the ratio of the true radiation stress to the narrow-banded radiation stress ($S_{xx}^{(tr)}/S_{xx}^{(nb)}$ and $S_{xy}^{(tr)}/S_{xy}^{(nb)}$). The use of a directional-frequency spectrum (symmetric or asymmetric) in the radiation stress calculations resulted in a decrease in the radiation stress components S_{xx} and S_{xy} when compared to the narrow-banded radiation stress approximation for all wave angles included in the analysis (excluding S_{xy} with $\theta_{po} = 0^0$, in which case all values were 0). For the S_{xx} component, the symmetric wave spectrum resulted in the lowest value in each case, with the percent change from the narrow-banded radiation stress value increasing with a decrease in the incident wave angle. When a symmetric wave spectrum was used in the radiation stress calculation, a larger percent change in S_{xx} was found in trials with high directional spread (with a maximum percent change of 10.47% in trials with high directional spread versus 7.13% from trials with low directional spread, both with $\theta_{po} = 0^0$). When an asymmetric wave spectrum was used, the percent decrease from the narrow-banded approximation dropped significantly, although the magnitude of this change was a function of directional spread (Figure 3).

Similar to the results presented by Feddersen (2004) and Battjes (1972), a much more significant discrepancy was seen in the values of the off-diagonal radiation stress component S_{xy} calculated using a narrow-banded radiation stress approximation and a symmetric frequency-directional spectrum. In this case, the inclusion of asymmetry resulted in a further decrease in the calculated radiation stress value when compared to the narrow-banded value for both sea states. The largest percent change was seen in trials with $\theta_{po} = 30^0$ and high

directional spread (42.3% decrease). When a symmetric frequency directional spectrum was used in calculations with the same input conditions, the percent change from the narrow-banded approximation decreased to 14.3%. Trials with low directional spread resulted in full-spectral S_{xy} values closer to the narrow-banded approximation for all sets of input conditions. Extended results are shown in Appendix E., Table 1.

The amount of directional spread in spectral formulations is controlled by the *s* parameter in the directional spreading function (shown in Equation 5). In the present study, two offshore s_{max} values were assessed, a high spreading case (s_{max} = 10) and a low spreading case (s_{max} = 75), selected to be consistent with the values used by Lee et al (2010). As Battjes (1972) and Feddersen (2004) demonstrated, the difference between the true radiation stress value and the narrow-banded approximation is dependent on the directional spread in the wave spectrum. The present results show that the importance of directional asymmetry in radiation stress calculations is also a function of directional spread. Although asymmetry was found to reduce the differences seen between the narrow-banded S_{xx} approximation and the full spectral S_{xx} calculated using a symmetric spectrum in both sea states, the difference between the S_{xx} values calculated from the symmetric and asymmetric spectra were significantly larger with an increase in directional spread. This same trend was found to be true in the calculation of S_{xy}.

Past studies have demonstrated that the inclusion of symmetric directional spreading in radiation stress calculations results in a decrease in both S_{xx} and S_{xy} (Battjes, 1972; Ruessink et al, 2001; Feddersen, 2004; and Puleo, 2010). The magnitude of S_{xy} outside of the surfzone has been empirically linked to the maximum longshore current velocity (Feddersen et al., 1998; Guza et al., 1986), and the importance of the inclusion of directional spreading in alongshore current and sediment transport calculation has been discussed in a number of studies (Ruessink et al., 2001; Puleo, 2010; and Barbaro et al., 2014). The present results suggest that the inclusion of a more realistic asymmetric directional spreading function in nearshore radiation stress calculations reduces the differences seen between the monochromatic S_{xx} approximation and the full spectral S_{xx} calculated using a symmetric spectrum, but increases the differences seen in S_{xy}, particularly in broad-banded seas. This suggests that the biases in longshore current velocities and sediment transport rates due to the use of the narrow-banded radiation stress approximation presented in past studies may in fact underestimate the actual difference due to the exclusion of directional asymmetry in the wave spectrum.

4. Conclusions

Gradients in wave radiation stresses are the main drivers behind many nearshore processes. To facilitate their calculation and use, radiation stresses are often approximated using a monochromatic radiation stress formulation, under the assumption that the sea state is narrow-banded in frequency and directional space and therefore the difference between the monochromatic formulation and the formulation for real seas is small. However, past studies have shown that the inclusion of directional spreading in radiation stress calculations can have a significant impact on the resulting values in seas with high directional spread. In this study, the importance of asymmetry in the directional distribution of spectral energy due to refraction in radiation stress calculations was investigated. Radiation stresses were calculated using a) a narrow-banded approximation (i.e. monochromatic waves), b) a symmetric frequency directional spectrum, and c) an asymmetric frequency directional spectrum. Results show that the inclusion of directional asymmetry results in an S_{xx} value closer to the narrow-banded approximations, but that it increases the differences between the true S_{xy} value and the narrow-banded approximation. Additionally, the differences between the radiation stress values calculated using a symmetric and asymmetric spectrum were found to increase with an increase in directional spread. These results suggest that the use of a narrow-banded radiation stress approximation in nearshore models could result in a significant overestimate of alongshore current velocities and longshore sediment transport rates, particularly in broad-banded seas.

Figures

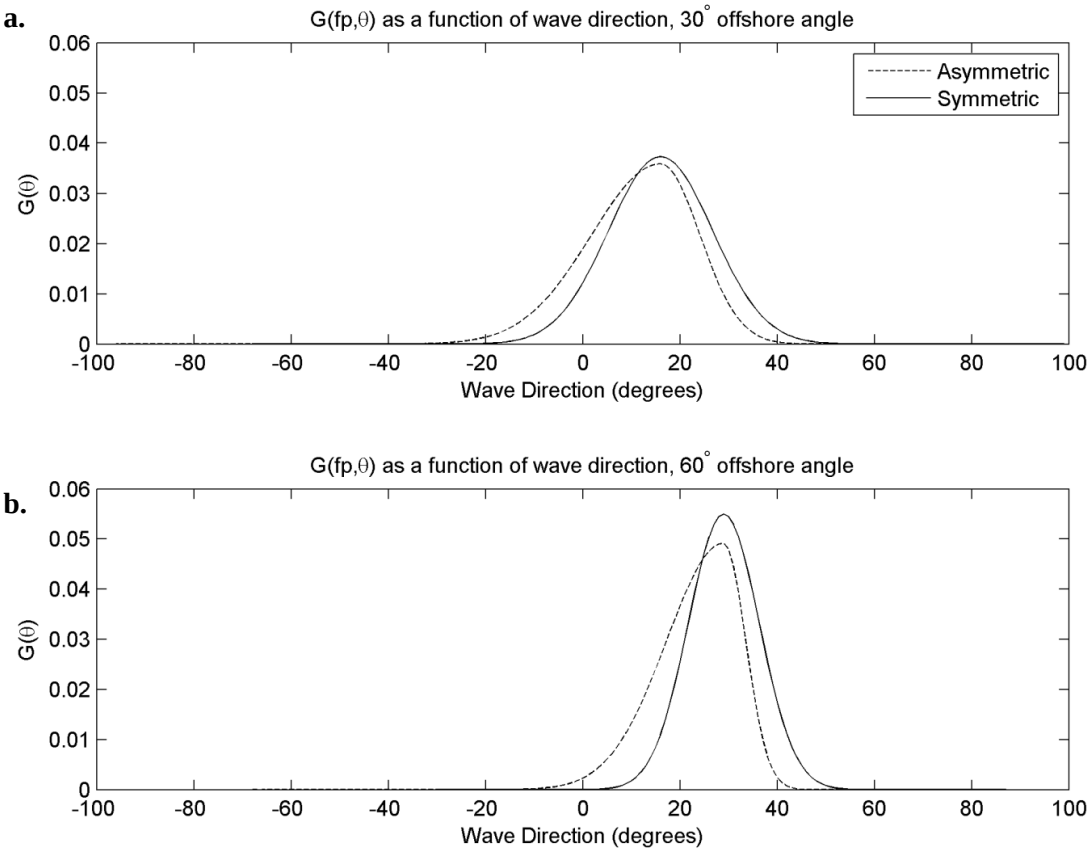

Figure 1. *G(f,θ)* at the peak frequency (f_p = 0.0934) from trials with high directional spread (offshore s_{max} = 10) as a function of wave direction with an offshore dominant wave direction of **a)** 30^0 and **b)** 60^0.

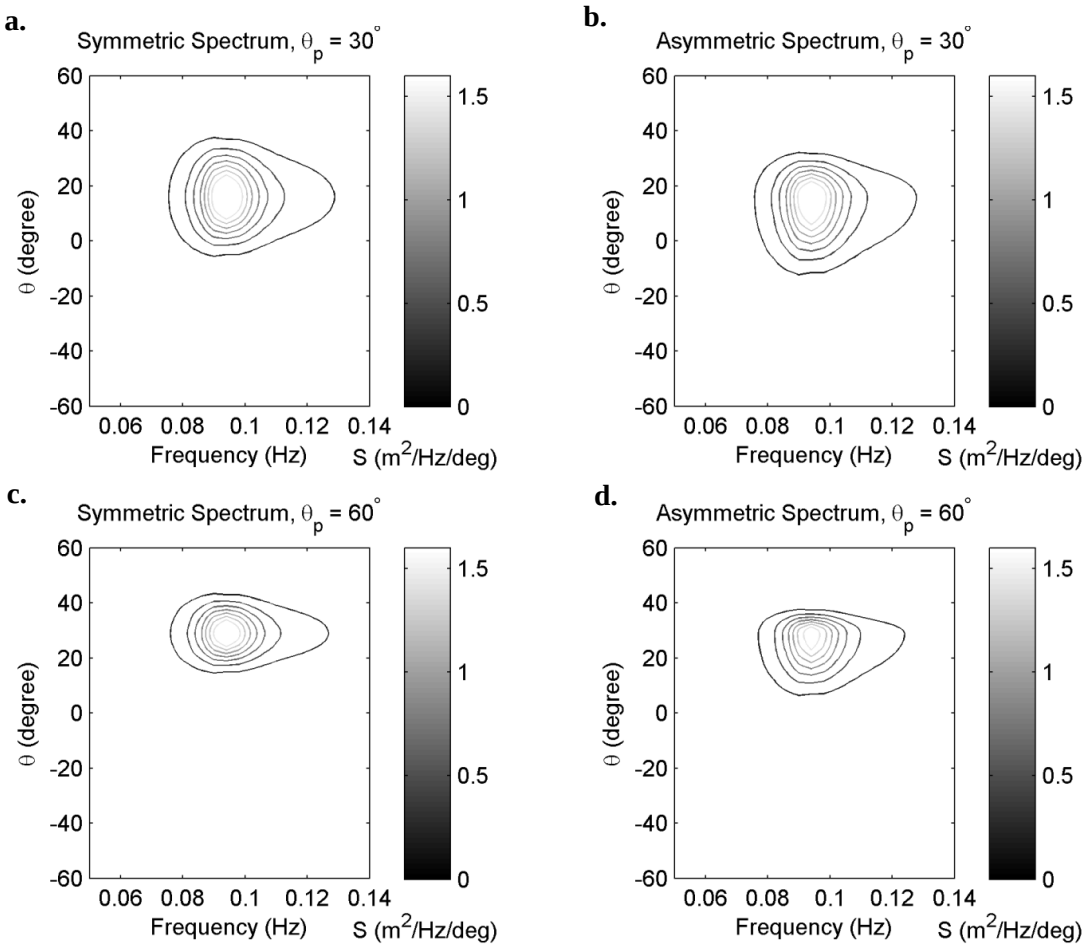

Figure 2. Frequency directional spectra *S(f,θ)* from cases with a) a symmetric spectrum and a 30^0 offshore dominant wave direction, b) an asymmetric spectrum and a 30^0 offshore dominant wave direction, c) a symmetric spectrum and a 60^0 offshore dominant wave direction, and d) an asymmetric spectrum and a 60^0 offshore dominant wave direction for high directional spread cases (offshore s_{max} = 10).

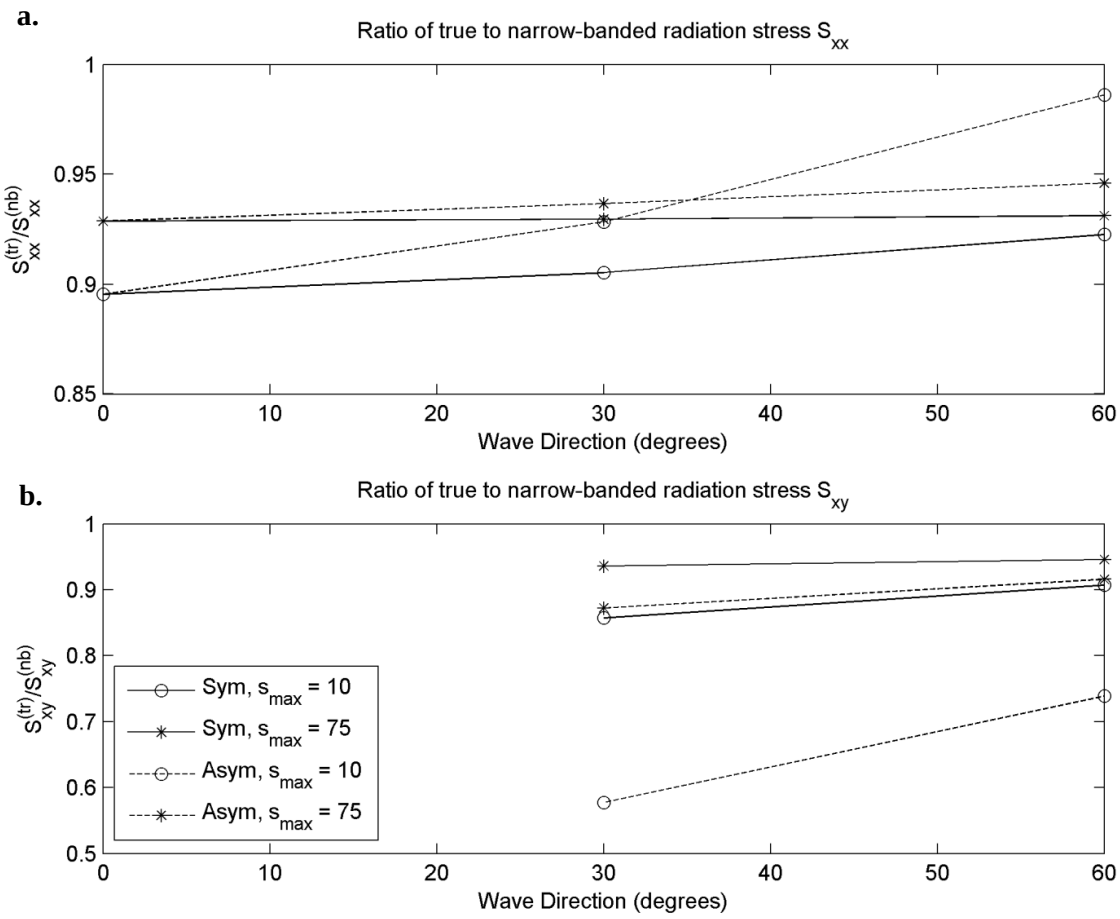

Figure 3. Ratio of true to narrow-banded a) S_{xx} ($S_{xx}^{(tr)}/S_{xx}^{(nb)}$) and b) S_{xy} ($S_{xy}^{(tr)}/S_{xy}^{(nb)}$) as a function of dominant offshore wave direction for both cases with high (offshore s_{max} = 10) and low (offshore s_{max} = 75) directional spread.

Tables

Table 1. Input conditions for all trials. An offshore significant wave height H_{so} of 5 m and a significant period T_s of 10 s were used in all calculations. An increase in s_{max} implies a decrease in directional spread.

	Offshore Θ (^{0})	**Offshore S_{max}**	**Asymmetry parameter μ**	**S_{max} at the 10 m contour line**
Asymmetric	0	10	0	55
	30	10	-0.28	69
	60	10	-0.48	150
	0	75	0	330
	30	75	-0.28	400
	60	75	-0.48	1000
Symmetric	0	10	0	55
	30	10	0	68
	60	10	0	120
	0	75	0	330
	30	75	0	400
	60	75	0	1000

Table 2. Input conditions, conditions at the 10 m contour line, and narrow-banded radiation stress values from all trials.

Offshore Θ (^{0})	**Offshore S_{max}**	**Θ 10 m contour (^{0})**	**H_s at 10 m contour (m)**	**$S_{xx}^{(nb)}/\rho$ (m^3/s^2)**	**$S_{xy}^{(nb)}/\rho$ (m^3/s^2)**
0	10, 75	0	5.03	19.78	0.00
30	10, 75	16	4.78	16.89	3.29
60	10, 75	29	3.80	9.44	3.33

References

Barbaro, G.; Foti, G.; Sicilia, L.; and Malara, G. 2014, "A Formula for the Calculation of the Longshore Sediment Transport Including Spectral Effects." J. of Coast. Res. 30 (5): 961-966.

Battjes, J.A. 1972, "Radiation Stress in short-crested waves." J. Mar. Res. 30 (1): 56-64.

Feddersen, F. 2004, "Effect of wave directional spread on radiation stress: comparing theory and observations." Coast. Eng. 51: 473-481.

Feddersen, F; Guza, R.T.; Elgar, S.; and Herbers, T.H.C. 1998, "Alongshore momentum balances in the nearshore," J. Geophys. Res. 103 (C8), pp. 15667-15676.

Goda, Y and Suzuki, Y. 1975, "Computation of refraction and diffraction of sea waves with Mitsuyasu's directional spectrum." Rep. No. 230. The Port and Harbour Research Institute, Japan (in Japanese).

Guza, R.T.; Thorton, E.B.; and Christensen Jr, N. 1986, "Observations of Steady Longshore Currents in the Surf Zone." J. Phys. Oceanogr. 16, pp. 1959-1969.

Herbers, T.H.C.; Elgar, S.; and Guza, R.T. 1999, "Directional spreading of waves in the nearshore." J. Geophys. Res. 104 (C4): 7683-7693

Higgins, A.L.; Seymour, R.J.; and Pawka, S.S. 1981, "A compact representation of ocean wave directionality." Appl. Ocean Res. 3(3): 105-112.

Komar, P.D. 1998, Beach Processes and Sedimentation, Prentice-Hall Inc, Upper Saddle River, NJ. 2nd Ed. Ch. 9.

Kumar, V.S.; Deo, M.C.; Anand, N.M.; and Chandramohan, P. 1999, "Technical Note: Estimation of wave directional spreading in shallow water." Ocean Eng. 26: 83-98.

Lee, C.; Jung, J.S., and Haller, M.C. 2010, "Asymmetry in directional spreading function of random waves due to refraction." J. Waterw. Port. C-ASCE 136 (1): 1-9.

Long, C.E and Oltman-Shay, J.M. 1991, "Directional characteristics of waves in shallow water." Technical Report CERC-91-1.

Longuet-Higgins, M.S. 1970, " Longshore Currents Generated by Obliquely Incident Sea Waves, 1." J. Geophys. Res. 75 (33): 6778 – 6789.

Longuet-Higgins, M.S. 1970, "Longshore Currents Generated by Obliquely Incident Sea Waves, 2." J. Geophys. Res. Research 75 (33): 6791 – 6801.

Longuet-Higgins, M.S.; Cartwright, D.E.; and Smith, N.D. 1963, "Observations of the directional spectrum of sea waves using the motion of a floating buoy." Ocean Wave Spectra. Prentice-Hall, Englewood Cliffs, NJ, 111-136.

Longuet-Higgins, M.S. and Stewart, R.W. 1960, “Changes in the form of short gravity waves on long waves and tidal currents.” J. Fluid Mech. (4): 565-583.

Longuet-Higgins, M.S. and Stewart, R.W. 1964, “Radiation stresses in water waves; a physical discussion, with applications.” Deep-Sea Res. 11: 529-562.

Mitsuyasu, H.; Tasai, F.; Suhara, T.; Mizuno, S.; Ohkusu, M.; Honda, T.; and Rikiishi, K. 1975, “Observations of the Directional Spectrum of Ocean Waves Using a Cloverleaf Buoy.” J. Phys. Oceanogr. 5: 750-760.

Puleo, J. 2010, “Estimating Alongshore Sediment Transport and the Nodal Point Location on the Delaware-Maryland Coast.” J. Waterw. Port. C-ASCE 136: 135-144.

Ruessink, B.G.; Miles, J.R.; Feddersen, F.; Guza, R.T.; and Elgar, S. 2001, “Modeling the Alongshore Current on Barred Beaches.” J. Geophys. Res., 106, 22451-22463.

Sundar, V.; Sannasiraj, S.A.; and Kaldenhoff, H. 1999, “Directional spreading of waves in the nearshore zone.” Ocean Eng. 26: 161-188.

Svendsen, I.A. 2006, Introduction to Nearshore Hydrodynamics, World Scientific Publishing Co. Pte. Ltd., Singapore, Chap. 11,12.

Thorton, E.B. and Guza, R.T. 1986, “Surf zone longshore currents and random waves: field data and models.” J. Phys. Oceanogr. 16: 1165-1178.

Combined References

Abanades, J.; Greaves, D.; and Iglesias, G. 2014a, "Wavefarm impact on the beach profile: A case study." Coast. Eng. 86, pp. 36-44.

Abanades, J.; Greaves, D.; and Iglesias, G. 2014b, "Coastal defence through wave farms." Coast. Eng. 91, pp 299-307.

Barbaro, G.; Foti, G.; Sicilia, L.; and Malara, G. 2014, "A Formula for the Calculation of the Longshore Sediment Transport Including Spectral Effects." J. of Coast. Res. 30 (5): 961-966.

Battjes, J.A. 1972, "Radiation Stress in short-crested waves." J. Mar. Res. 30 (1): 56-64.

Booij, N.; Ris, R.C.; Holthuijsen, L.H. 1999, "A third-generation wave model for coastal regions: 1. Model description and validation." J. Geophys. Res. Oceans 104 (C4), pp. 7649-7666.

Bowen, A.J. 1969, "Rip Currents 1. Theoretical Investigations." J. Geophys. Res. 74 (23), pp. 5467-5478.

Carballo, R. and Iglesias, G., 2013. "Wave farm impact based on realistic wave-WEC interactions," Energy 51, pp. 216-219.

Carignan, K.S.; Taylor, L.A.; Eakins, B.W.; Warnken, R.R.; Lim, E.; and Medley, P.R. 2009, "Digital Elevation Model of Central Oregon Coast: Procedures, Data Sources and Analysis," NOAA Technical Memorandum NESDIS NGDC-25, U.S. Dept. of Commerce, Boulder, CO, 38 pp.

Dean, R.G. and Dalrymple, R.A. 2010, Water Wave Mechanics for Engineers and Scientists. World Scientific Publishing Co. Pte. Ltd., Singapore, Chap. 4.

Feddersen, F. 2004, "Effect of wave directional spread on radiation stress: comparing theory and observations." Coast. Eng. 51: 473-481.

Feddersen, F; Guza, R.T; Elgar, S.; and Herbers, T.H.C. 1998, "Alongshore momentum balances in the nearshore," J. Geophys. Res. 103 (C8), pp. 15667-15676.

Garcia-Medina, G.; Ozkan-Haller, H.T.; Ruggiero, P.; and Oskamp, J. 2013, "An inner-shelf wave forecasting system for the US Pacific Northwest," Weather Forecast. 28, pp. 681-703.

Goda, Y and Suzuki, Y. 1975, "Computation of refraction and diffraction of sea waves with Mitsuyasu's directional spectrum." Rep. No. 230. The Port and Harbour Research Institute, Japan (in Japanese).

Gonzalez-Santamaria, R.; Zou, Q.P.; and Pan, S. 2013, "Impacts of a wave farm on waves, currents and coastal morphology in South West England," Estuar. Coasts 1, pp. 1-14.

Guza, R.T.; Thorton, E.B.; and Christensen Jr, N. 1986, "Observations of Steady Longshore Currents in the Surf Zone." J. Phys. Oceanogr. 16, pp. 1959-1969.

Herbers, T.H.C.; Elgar, S.; and Guza, R.T. 1999, "Directional spreading of waves in the nearshore." J. Geophys. Res. 104 (C4): 7683-7693

Higgins, A.L.; Seymour, R.J.; and Pawka, S.S. 1981, "A compact representation of ocean wave directionality." Appl. Ocean Res. 3(3): 105-112.

Holthuijsen, L.H.; Herman, A.; and Booij, N. 2003, "Phase-decoupled refraction-diffraction for spectral wave models." Coast. Eng. 49, pp. 291-305.

Komar, P.D. 1998, Beach Processes and Sedimentation, Prentice-Hall Inc, Upper Saddle River, NJ. 2nd Ed. Ch. 9.

Kumar, V.S.; Deo, M.C.; Anand, N.M.; and Chandramohan, P. 1999, "Technical Note: Estimation of wave directional spreading in shallow water." Ocean Eng. 26: 83-98.

Lee, C.; Jung, J.S., and Haller, M.C. 2010, "Asymmetry in directional spreading function of random waves due to refraction." J. Waterw. Port. C-ASCE 136 (1): 1-9.

Lenee-Bluhm, P.; Paasch, R.; and Ozkan-Haller, H.T. 2011. "Characterizing the wave energy resource of the US Pacific Northwest." Renew. Energ. 36, pp. 2106-2119.

Long, C.E and Oltman-Shay, J.M. 1991, "Directional characteristics of waves in shallow water." Technical Report CERC-91-1.

Longuet-Higgins, M.S. 1970, " Longshore Currents Generated by Obliquely Incident Sea Waves, 1." J. Geophys. Res. 75 (33): 6778 – 6789.

Longuet-Higgins, M.S. 1970, "Longshore Currents Generated by Obliquely Incident Sea Waves, 2." J. Geophys. Res. Research 75 (33): 6791 – 6801.

Longuet-Higgins, M.S.; Cartwright, D.E.; and Smith, N.D. 1963, "Observations of the directional spectrum of sea waves using the motion of a floating buoy." Ocean Wave Spectra. Prentice-Hall, Englewood Cliffs, NJ, 111-136.

Longuet-Higgins, M.S. and Stewart, R.W. 1960, "Changes in the form of short gravity waves on long waves and tidal currents." J. Fluid Mech. (4): 565-583.

Longuet-Higgins, M.S. and Stewart, R.W. 1964, "Radiation stresses in water waves; a physical discussion, with applications." Deep-Sea Res. 11: 529-562.

Mendoza, E.; Silva, R.; Zanuttigh, B.; Angelilli, E.; Andersen, T.L.; Marinelli, L.; Norgaard, J.Q.H.; and Ruol, P. 2013, "Beach response to wave energy converter farms acting as coastal defence." Coast. Eng. 87, pp 97-111

Millar, D.L.; Smith, H.C.M; and Reeve, D.E. 2007, "Modelling analysis of the sensitivity of shoreline change to a wave farm," Oc. Eng. 34, pp. 884-901.

Mitsuyasu, H.; Tasai, F.; Suhara, T.; Mizuno, S.; Ohkusu, M.; Honda, T.; and Rikiishi, K. 1975, "Observations of the Directional Spectrum of Ocean Waves Using a Cloverleaf Buoy." J. Phys. Oceanogr. 5: 750-760.

Palha, A.; Mendes, L.; Fortes, C.J.; Brito-Melo, A.; and Sarmento, A. 2010, "The impact of wave energy farms in the shoreline wave climate: Portuguese pilot zone case study using Pelamis energy wave devices." Renew. Energ. 35, pp. 62-77.

Puleo, J. 2010, "Estimating Alongshore Sediment Transport and the Nodal Point Location on the Delaware-Maryland Coast." J. Waterw. Port. C-ASCE 136: 135-144.

Rhinefrank, K., M. Haller, T. Ozkan-Haller, A. Porter, C. McNatt, P. Lenee-Bluhm, and Schumacher, E. 2013, Benchmark Modeling of the Near-Field and Far-Field Wave Effects of Wave Energy Arrays, Columbia Power Technologies Final Report, DE-EE0002658, U.S. Dept. of Energy, www.osti.gov/servlets/purl/1060889/.

Ruessink, B.G.; Miles, J.R.; Feddersen, F.; Guza, R.T.; and Elgar, S. 2001, "Modeling the Alongshore Current on Barred Beaches." J. Geophys. Res., 106, 22451-22463.

Rusu, E. and Soares, C.G. 2013, "Coastal impact induced by a Pelamis wave farm operating in the Portuguese nearshore," Renew. Energ. 58, pp. 34-49.

Smith, H.C.M.; Pearce, C.; and Millar, D.L, 2012. "Further analysis of change in nearshore wave climate due to an offshore wave farm: An enhanced case study for the Wave Hub site." Renew. Energ. 40, pp. 51-64.

Sundar, V.; Sannasiraj, S.A.; and Kaldenhoff, H. 1999, "Directional spreading of waves in the nearshore zone." Ocean Eng. 26: 161-188.

Svendsen, I.A, 2006, Introduction to Nearshore Hydrodynamics, World Scientific Publishing Co. Pte. Ltd., Singapore, Chap. 11,12.

SWAN team. 2006a, "SWAN Technical Documentation." Delft University of Technology.

SWAN team. 2006b, "SWAN User Manual." Delft University of Technology.

Thorton, E.B. and Guza, R.T. 1986, "Surf zone longshore currents and random waves: field data and models." J. Phys. Oceanogr. 16: 1165-1178.

Vardaro, M.; Risien, C.; Wingard, C.; and Fram, J. 2011, In-Shore Mooring Test 2 (ISMT2) Science Data Report, Oregon State University, Coastal and Global Scale Nodes, Ocean Observatories Initiative.

APPENDICES

Appendix A: Directional Resolution

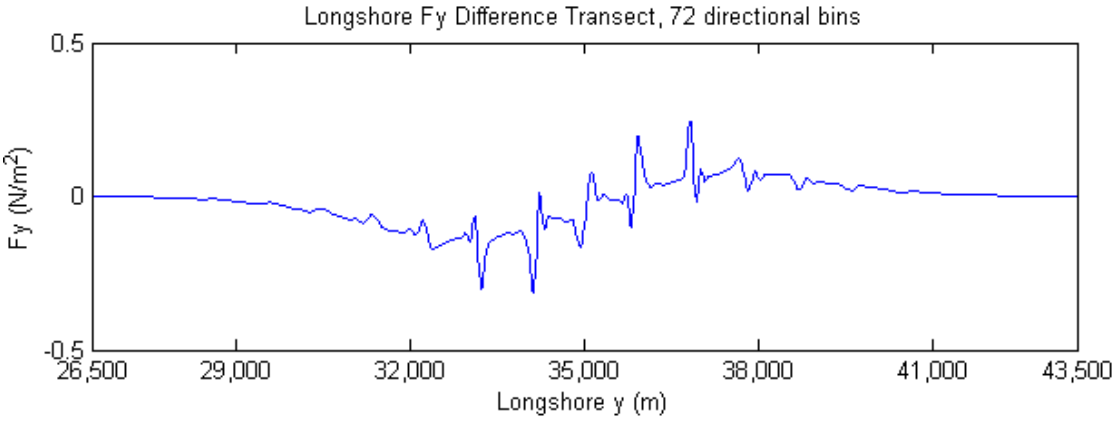

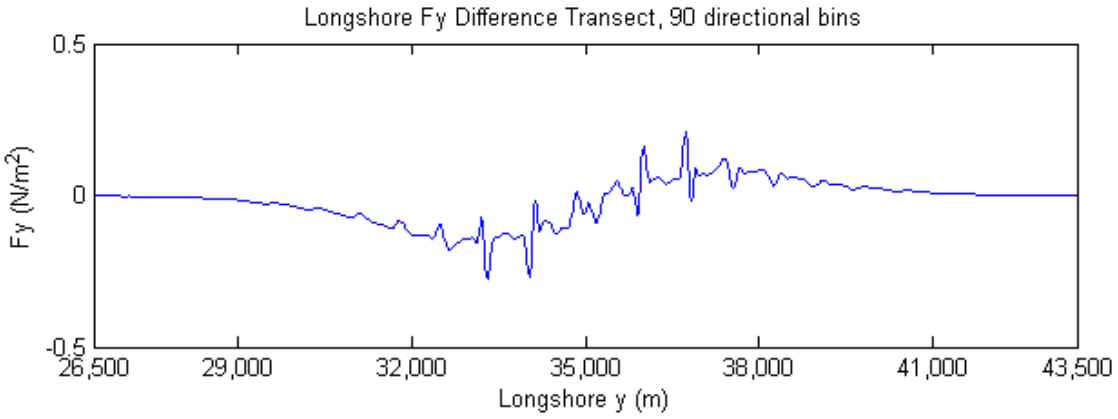

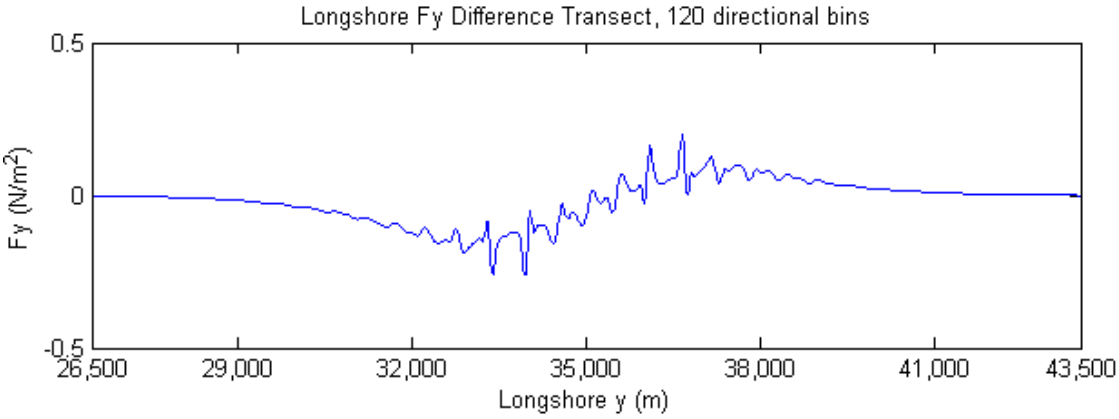

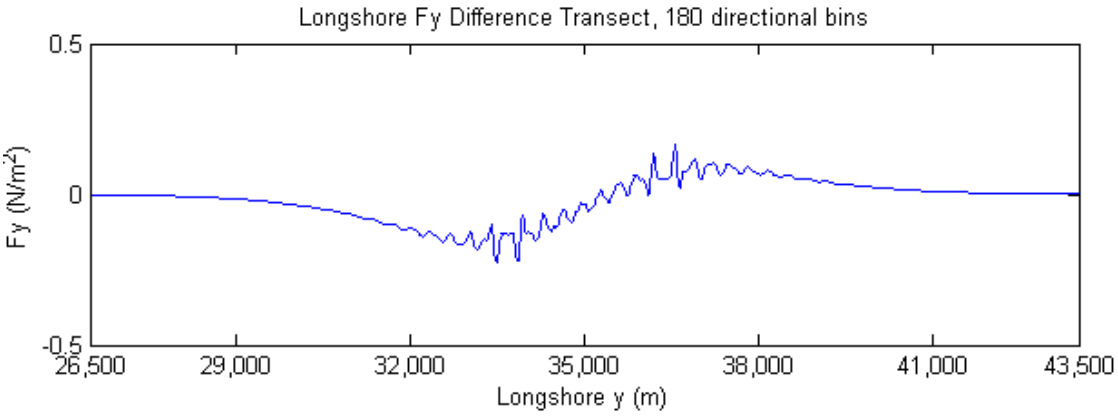
Longshore Fy Difference Transect, 180 directional bins
0.5
0
-0.5
Fy (N/m²)
26,500
29,000
32,000
35,000
38,000
41,000
43,500
Longshore y (m)

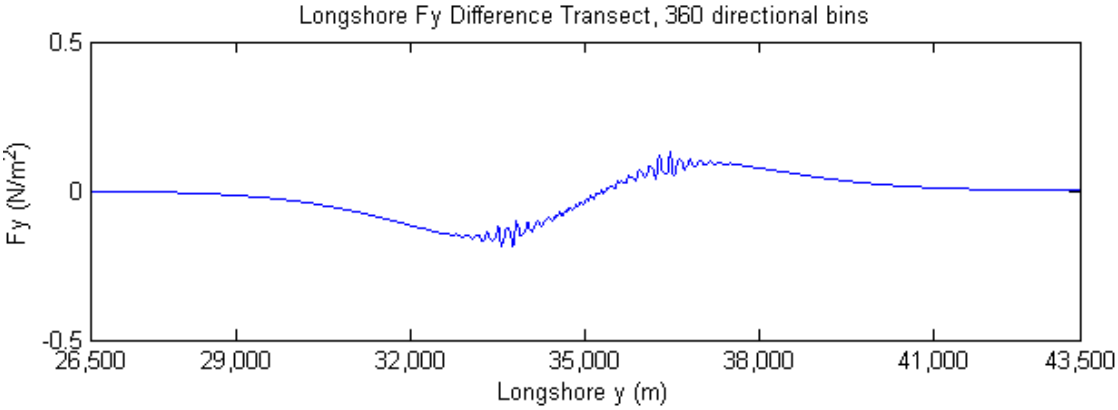
Longshore Fy Difference Transect, 360 directional bins
0.5
0
-0.5
Fy (N/m²)
26,500
29,000
32,000
35,000
38,000
41,000
43,500
Longshore y (m)

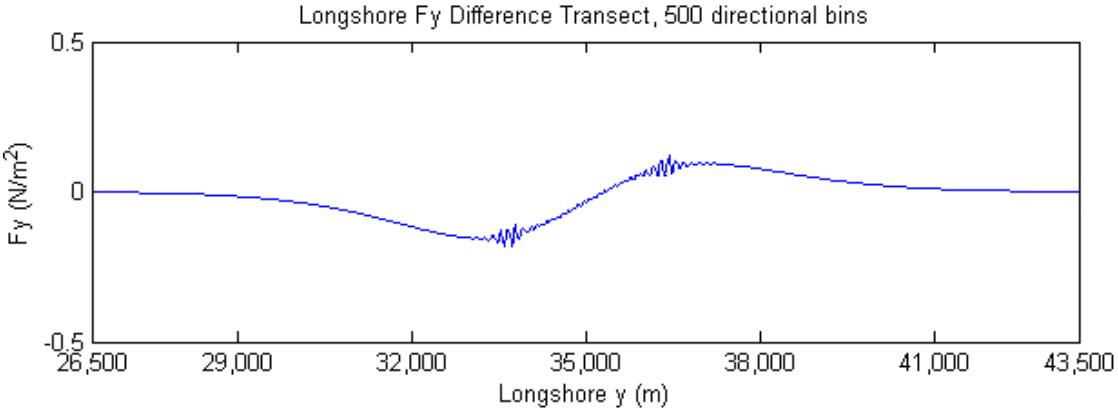
Longshore Fy Difference Transect, 500 directional bins
0.5
0
-0.5
Fy (N/m²)
26,500
29,000
32,000
35,000
38,000
41,000
43,500
Longshore y (m)

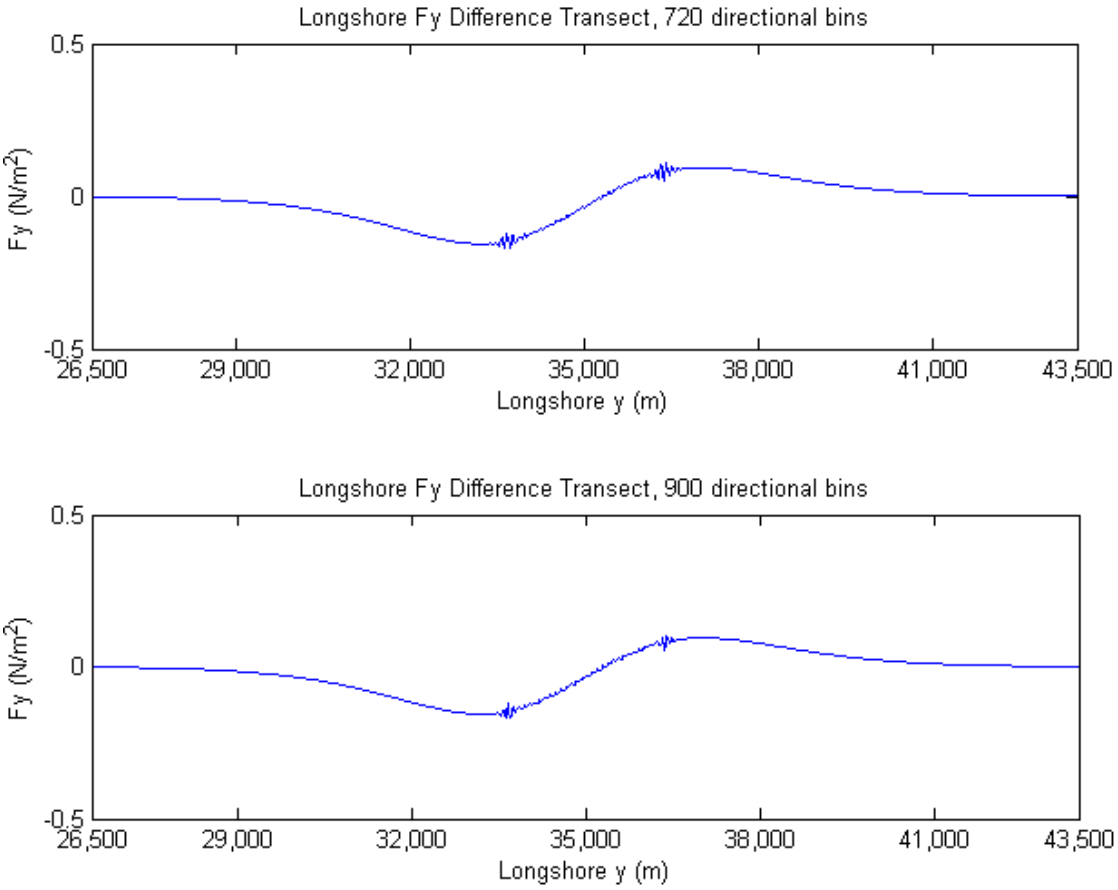

Figure 1. Longshore transects of the difference in F_y at the location of maximum dissipation for trials with increasing directional resolution, from 72 directional bins to 900 directional bins.

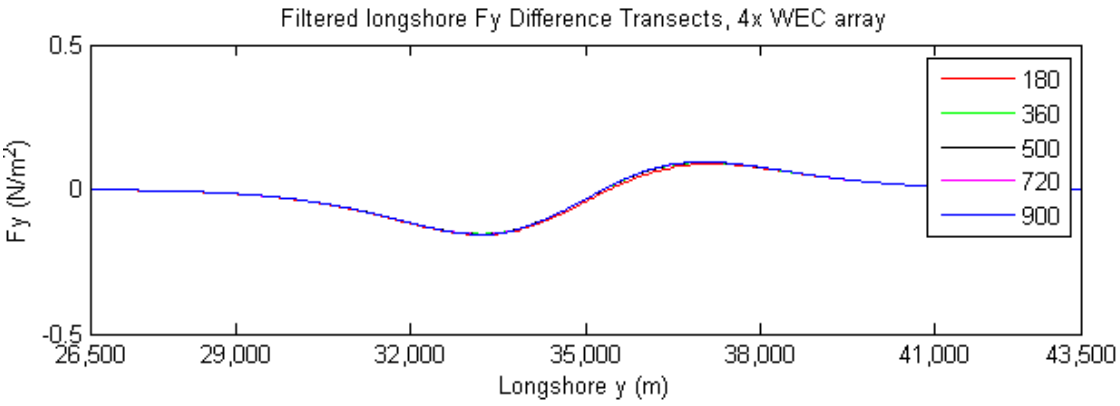

a.

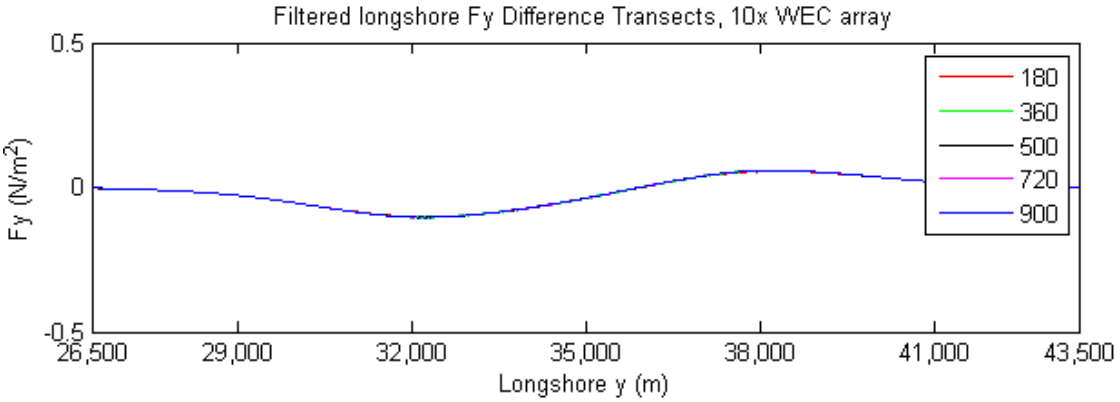

b,

Figure 2. Filtered longshore transects of the difference in F_y at the location of maximum dissipation for trials with increasing directional resolution, with **a)** a closely-spaced array and **b)** a widely-spaced array. Transects were filtered with a 270 m spatial filter.

Appendix B. Extended results from parametric study.

Table 1. Results from trials with a widely-spaced array located 5 km from shore.

	Widely-spaced WEC array (10x)							
Run	**Hs (m)**	**Tp (s)**	**Directional Spread (°)**	**Fy Difference (N/m3)**	**Fx Difference (N/m3)**	**% Difference Fx**	**Hs difference (m)**	**% Difference Hs**
1	2	6	14	0.01	0.05	0.64	0.01	0.52
2	6	6	14	0.02	0.08	0.68	0.02	0.32
3	2	7	14	0.03	0.21	2.34	0.05	2.48
4	6	7	14	0.09	0.32	2.19	0.11	1.92
5	2	8	14	0.05	0.35	3.55	0.08	4.28
6	6	8	14	0.16	0.56	3.23	0.20	3.71
7	2	9	14	0.06	0.48	4.38	0.12	5.69
8	6	9	14	0.21	0.80	3.99	0.29	5.25
9	2	10	14	0.06	0.59	5.02	0.12	5.94
10	6	10	14	0.23	0.95	4.21	0.32	5.77
11	2	12	14	0.06	0.54	4.06	0.12	5.26
12	6	12	14	0.23	0.98	3.64	0.32	5.51
13	2	14	14	0.06	0.59	3.97	0.11	4.51
14	6	14	14	0.22	0.99	3.23	0.30	5.01
15	2	16	14	0.06	0.59	3.69	0.10	4.21
16	6	16	14	0.22	1.09	3.24	0.30	4.86
17	2	18	14	0.05	0.58	3.39	0.10	3.73
18	6	18	14	0.22	1.18	3.22	0.28	4.42
19	2	6	35	0.02	0.02	0.28	0.00	0.00
20	6	6	35	0.03	0.05	0.56	0.01	0.15
21	2	7	35	0.04	0.13	1.61	0.03	1.48
22	6	7	35	0.14	0.20	1.64	0.05	1.05
23	2	8	35	0.07	0.22	2.47	0.05	2.66
24	6	8	35	0.25	0.39	2.57	0.12	2.27
25	2	9	35	0.09	0.31	3.11	0.07	3.67
26	6	9	35	0.33	0.54	3.06	0.18	3.48
27	2	10	35	0.10	0.40	3.75	0.08	4.00
28	6	10	35	0.32	0.64	3.23	0.21	4.08
29	2	12	35	0.09	0.40	3.31	0.08	3.85
30	6	12	35	0.32	0.71	2.96	0.23	4.30
31	2	14	35	0.09	0.40	2.96	0.08	3.55
32	6	14	35	0.31	0.77	2.81	0.23	4.18
33	2	16	35	0.08	0.52	3.52	0.08	3.54
34	6	16	35	0.29	0.92	3.01	0.24	4.29
35	2	18	35	0.08	0.52	3.33	0.08	3.26
36	6	18	35	0.27	1.02	3.06	0.24	4.03

Table 2. Results from trials with a closely-spaced array located 5 km from shore.

	Closely-spaced WEC array (4x)							
Run	**Hs (m)**	**Tp (s)**	**Directional Spread (^{0})**	**Fy difference (N/m^3)**	**Fx difference (N/m^3)**	**% Difference Fx**	**Hs difference (m)**	**% Difference Hs**
1	2	6	14	0.01	0.09	1.14	0.02	0.91
2	6	6	14	0.05	0.14	1.25	0.03	0.60
3	2	7	14	0.06	0.39	4.34	0.09	4.48
4	6	7	14	0.21	0.60	4.17	0.21	3.75
5	2	8	14	0.11	0.69	6.91	0.16	8.00
6	6	8	14	0.36	1.04	5.98	0.41	7.43
7	2	9	14	0.14	0.97	8.89	0.22	11.02
8	6	9	14	0.47	1.54	7.71	0.60	10.78
9	2	10	14	0.15	1.02	8.74	0.25	11.73
10	6	10	14	0.52	1.64	7.34	0.66	11.94
11	2	12	14	0.14	1.17	8.78	0.24	10.89
12	6	12	14	0.54	1.74	6.56	0.67	11.73
13	2	14	14	0.14	1.11	7.58	0.23	9.79
14	6	14	14	0.52	2.08	6.85	0.65	10.99
15	2	16	14	0.12	1.10	6.94	0.22	9.06
16	6	16	14	0.51	2.25	6.72	0.64	10.48
17	2	18	14	0.12	1.29	7.53	0.21	8.25
18	6	18	14	0.51	2.41	6.63	0.62	9.77
19	2	6	35	0.02	0.03	0.38	0.00	0.00
20	6	6	35	0.05	0.07	0.73	0.01	0.19
21	2	7	35	0.05	0.16	2.06	0.03	1.81
22	6	7	35	0.19	0.28	2.27	0.07	1.29
23	2	8	35	0.09	0.29	3.18	0.06	3.29
24	6	8	35	0.35	0.50	3.32	0.15	2.84
25	2	9	35	0.12	0.40	4.04	0.09	4.58
26	6	9	35	0.45	0.76	4.31	0.23	4.40
27	2	10	35	0.13	0.43	4.04	0.10	5.02
28	6	10	35	0.43	0.81	4.07	0.27	5.19
29	2	12	35	0.14	0.54	4.41	0.10	4.95
30	6	12	35	0.51	1.00	4.17	0.30	5.62
31	2	14	35	0.14	0.55	4.07	0.10	4.72
32	6	14	35	0.54	1.11	4.04	0.31	5.72
33	2	16	35	0.14	0.60	4.12	0.11	4.82
34	6	16	35	0.55	1.19	3.90	0.34	6.06
35	2	18	35	0.13	0.76	4.84	0.11	4.68
36	6	18	35	0.56	1.37	4.12	0.35	6.06

Table 3. Results from trials with a widely-spaced array located 10 km from shore.

	Widely-spaced WEC array (10x)							
Run	**Hs (m)**	**Tp (s)**	**Directional Spread (°)**	**Fy Difference (N/m3)**	**Fx Difference (N/m3)**	**% Difference Fx**	**Hs difference (m)**	**% Difference Hs**
1	2	6	14	0.01	0.04	0.52	0.01	0.40
2	6	6	14	0.02	0.07	0.62	0.01	0.26
3	2	7	14	0.02	0.17	1.92	0.04	1.91
4	6	7	14	0.09	0.30	2.07	0.08	1.54
5	2	8	14	0.04	0.29	2.95	0.07	3.34
6	6	8	14	0.16	0.57	3.15	0.16	2.98
7	2	9	14	0.05	0.40	3.64	0.09	4.51
8	6	9	14	0.21	0.82	3.94	0.24	4.27
9	2	10	14	0.06	0.50	4.20	0.10	4.76
10	6	10	14	0.20	0.88	3.92	0.26	4.74
11	2	12	14	0.05	0.46	3.47	0.10	4.33
12	6	12	14	0.19	0.92	3.42	0.26	4.64
13	2	14	14	0.05	0.51	3.46	0.09	3.83
14	6	14	14	0.18	0.94	3.08	0.26	4.34
15	2	16	14	0.05	0.54	3.35	0.09	3.71
16	6	16	14	0.17	1.07	3.17	0.27	4.34
17	2	18	14	0.04	0.53	3.10	0.09	3.40
18	6	18	14	0.17	1.13	3.11	0.26	4.10
19	2	6	35	0.03	0.00	0.02	-0.01	-0.35
20	6	6	35	0.02	0.08	0.83	-0.01	-0.26
21	2	7	35	0.03	0.04	0.47	0.00	0.08
22	6	7	35	0.08	0.15	1.20	0.00	0.01
23	2	8	35	0.04	0.08	0.85	0.01	0.52
24	6	8	35	0.16	0.23	1.49	0.02	0.39
25	2	9	35	0.06	0.11	1.12	0.02	0.89
26	6	9	35	0.21	0.31	1.70	0.04	0.78
27	2	10	35	0.06	0.11	1.08	0.02	1.01
28	6	10	35	0.23	0.34	1.67	0.05	0.96
29	2	12	35	0.06	0.12	1.03	0.02	0.95
30	6	12	35	0.20	0.32	1.33	0.05	1.01
31	2	14	35	0.05	0.12	0.89	0.02	0.88
32	6	14	35	0.19	0.31	1.16	0.05	1.01
33	2	16	35	0.05	0.17	1.18	0.02	1.05
34	6	16	35	0.19	0.39	1.28	0.07	1.26
35	2	18	35	0.05	0.18	1.19	0.02	1.06
36	6	18	35	0.19	0.43	1.31	0.08	1.33

Table 4. Results from trials with a closely-spaced array located 10 km from shore.

	Closely-spaced WEC array (4x)							
Run	**Hs (m)**	**Tp (s)**	**Directional Spread (^{0})**	**Fy difference (N/m^3)**	**Fx difference (N/m^3)**	**% Difference Fx**	**Hs difference (m)**	**% Difference Hs**
1	2	6	14	0.01	0.05	0.62	0.01	0.49
2	6	6	14	0.03	0.08	0.73	0.02	0.33
3	2	7	14	0.04	0.20	2.30	0.05	2.38
4	6	7	14	0.15	0.35	2.35	0.11	1.97
5	2	8	14	0.06	0.35	3.55	0.08	4.20
6	6	8	14	0.28	0.64	3.59	0.21	3.87
7	2	9	14	0.08	0.48	4.45	0.12	5.73
8	6	9	14	0.39	0.95	4.55	0.31	5.61
9	2	10	14	0.09	0.62	5.25	0.13	6.10
10	6	10	14	0.32	1.02	4.52	0.35	6.26
11	2	12	14	0.09	0.60	4.47	0.13	5.68
12	6	12	14	0.32	1.09	4.06	0.36	6.25
13	2	14	14	0.08	0.69	4.65	0.12	5.19
14	6	14	14	0.31	1.16	3.81	0.36	6.01
15	2	16	14	0.08	0.73	4.55	0.13	5.07
16	6	16	14	0.31	1.36	4.03	0.37	6.06
17	2	18	14	0.08	0.74	4.33	0.12	4.79
18	6	18	14	0.31	1.49	4.09	0.37	5.89
19	2	6	35	0.03	0.00	0.02	-0.01	-0.35
20	6	6	35	0.02	0.08	0.83	-0.01	-0.26
21	2	7	35	0.03	0.04	0.47	0.00	0.12
22	6	7	35	0.09	0.14	1.12	0.00	0.04
23	2	8	35	0.04	0.08	0.85	0.01	0.60
24	6	8	35	0.16	0.22	1.43	0.02	0.47
25	2	9	35	0.05	0.11	1.13	0.02	1.02
26	6	9	35	0.22	0.30	1.66	0.04	0.91
27	2	10	35	0.06	0.12	1.10	0.02	1.14
28	6	10	35	0.23	0.34	1.63	0.05	1.11
29	2	12	35	0.05	0.13	1.13	0.02	1.08
30	6	12	35	0.20	0.30	1.28	0.06	1.17
31	2	14	35	0.05	0.13	0.99	0.02	1.00
32	6	14	35	0.19	0.30	1.12	0.06	1.17
33	2	16	35	0.06	0.19	1.34	0.03	1.17
34	6	16	35	0.19	0.39	1.29	0.08	1.43
35	2	18	35	0.06	0.21	1.34	0.03	1.18
36	6	18	35	0.20	0.45	1.36	0.09	1.50

Table 5. Results from trials with a widely-spaced array located 15 km from shore.

	Widely-spaced WEC array (10x)							
Run	**Hs (m)**	**Tp (s)**	**Directional Spread (°)**	**Fy Difference (N/m3)**	**Fx Difference (N/m3)**	**% Difference Fx**	**Hs difference (m)**	**% Difference Hs**
1	2	6	14	0.00	0.02	0.30	0.00	0.23
2	6	6	14	0.02	0.04	0.35	0.01	0.15
3	2	7	14	0.02	0.10	1.07	0.02	1.10
4	6	7	14	0.07	0.16	1.11	0.05	0.89
5	2	8	14	0.03	0.16	1.64	0.04	1.92
6	6	8	14	0.13	0.30	1.68	0.09	1.73
7	2	9	14	0.04	0.26	2.40	0.05	2.59
8	6	9	14	0.18	0.43	2.08	0.14	2.50
9	2	10	14	0.05	0.28	2.36	0.06	2.75
10	6	10	14	0.19	0.53	2.25	0.15	2.79
11	2	12	14	0.04	0.26	1.98	0.06	2.53
12	6	12	14	0.18	0.51	1.83	0.16	2.77
13	2	14	14	0.04	0.30	2.02	0.05	2.27
14	6	14	14	0.14	0.56	1.84	0.15	2.62
15	2	16	14	0.04	0.33	2.05	0.06	2.30
16	6	16	14	0.15	0.67	1.99	0.17	2.75
17	2	18	14	0.04	0.33	1.96	0.06	2.17
18	6	18	14	0.14	0.67	1.84	0.17	2.66
19	2	6	35	0.00	0.00	-0.03	-0.01	-0.40
20	6	6	35	0.01	0.07	0.73	-0.01	-0.30
21	2	7	35	0.02	0.00	-0.01	0.00	-0.24
22	6	7	35	0.06	0.09	0.73	-0.01	-0.24
23	2	8	35	0.03	0.01	0.14	0.00	-0.07
24	6	8	35	0.12	0.10	0.65	-0.01	-0.12
25	2	9	35	0.04	0.03	0.26	0.00	0.09
26	6	9	35	0.15	0.12	0.65	0.00	0.03
27	2	10	35	0.04	0.03	0.25	0.00	0.14
28	6	10	35	0.16	0.12	0.56	0.00	0.09
29	2	12	35	0.04	0.02	0.18	0.00	0.12
30	6	12	35	0.16	0.10	0.38	0.01	0.11
31	2	14	35	0.04	0.02	0.16	0.00	0.11
32	6	14	35	0.14	0.08	0.29	0.01	0.12
33	2	16	35	0.04	0.03	0.21	0.00	0.17
34	6	16	35	0.12	0.09	0.29	0.01	0.21
35	2	18	35	0.04	0.04	0.23	0.00	0.19
36	6	18	35	0.12	0.10	0.30	0.01	0.24

Table 6. Results from trials with a closely-spaced array located 15 km from shore.

	Closely-spaced WEC array (4x)							
Run	**Hs (m)**	**Tp (s)**	**Directional Spread (^{0})**	**Fy difference (N/m^3)**	**Fx difference (N/m^3)**	**% Difference Fx**	**Hs difference (m)**	**% Difference Hs**
1	2	6	14	0.00	0.03	0.37	0.01	0.28
2	6	6	14	0.02	0.05	0.47	0.01	0.18
3	2	7	14	0.02	0.11	1.29	0.03	1.32
4	6	7	14	0.10	0.22	1.51	0.06	1.08
5	2	8	14	0.04	0.19	1.95	0.05	2.32
6	6	8	14	0.18	0.41	2.27	0.12	2.11
7	2	9	14	0.05	0.32	2.96	0.06	3.16
8	6	9	14	0.24	0.58	2.80	0.17	3.05
9	2	10	14	0.06	0.35	2.94	0.07	3.35
10	6	10	14	0.25	0.62	2.66	0.19	3.41
11	2	12	14	0.05	0.33	2.50	0.07	3.09
12	6	12	14	0.24	0.65	2.32	0.19	3.39
13	2	14	14	0.05	0.39	2.62	0.07	2.80
14	6	14	14	0.18	0.72	2.36	0.19	3.24
15	2	16	14	0.05	0.41	2.59	0.07	2.81
16	6	16	14	0.18	0.76	2.27	0.21	3.36
17	2	18	14	0.05	0.42	2.47	0.07	2.67
18	6	18	14	0.18	0.85	2.35	0.21	3.29
19	2	6	35	0.00	0.00	-0.02	-0.01	-0.39
20	6	6	35	0.01	0.07	0.75	-0.01	-0.29
21	2	7	35	0.02	0.00	0.05	0.00	-0.19
22	6	7	35	0.06	0.10	0.78	-0.01	-0.20
23	2	8	35	0.03	0.02	0.25	0.00	0.04
24	6	8	35	0.11	0.12	0.76	0.00	-0.03
25	2	9	35	0.04	0.04	0.41	0.00	0.25
26	6	9	35	0.15	0.16	0.89	0.01	0.17
27	2	10	35	0.04	0.04	0.41	0.01	0.30
28	6	10	35	0.16	0.17	0.80	0.01	0.25
29	2	12	35	0.03	0.03	0.28	0.01	0.25
30	6	12	35	0.15	0.14	0.56	0.01	0.25
31	2	14	35	0.03	0.04	0.33	0.00	0.21
32	6	14	35	0.14	0.12	0.42	0.01	0.23
33	2	16	35	0.03	0.05	0.34	0.01	0.25
34	6	16	35	0.12	0.13	0.44	0.02	0.30
35	2	18	35	0.03	0.05	0.33	0.01	0.27
36	6	18	35	0.12	0.15	0.46	0.02	0.33

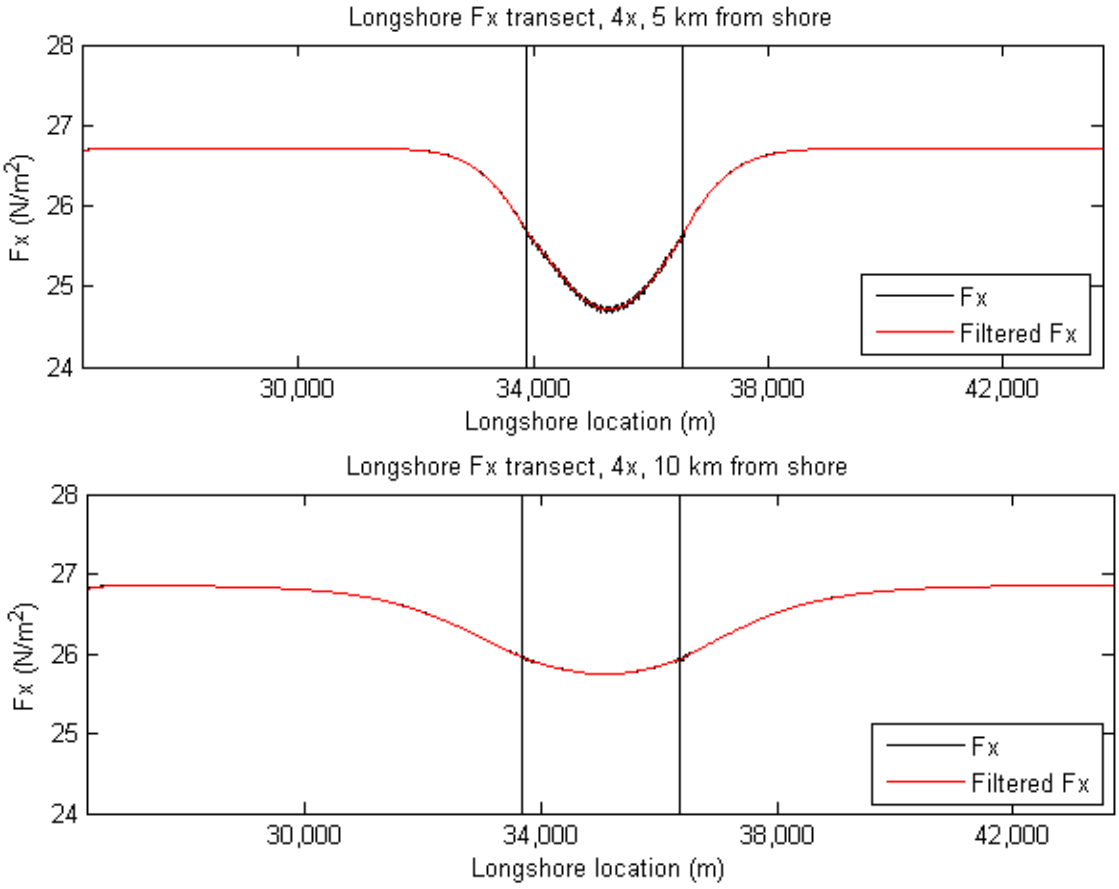

Figure 1. Longshore F_x transects in the lee of a closely-spaced array located **a)** 5 km and **b)** 10 km from shore with an input H_s = 6 m, an input T_p = 12 s, and low directional spread (14^0). The transect was taken from the location of the maximum F_x. The vertical black lines show the longshore location of the edges of the WEC array.

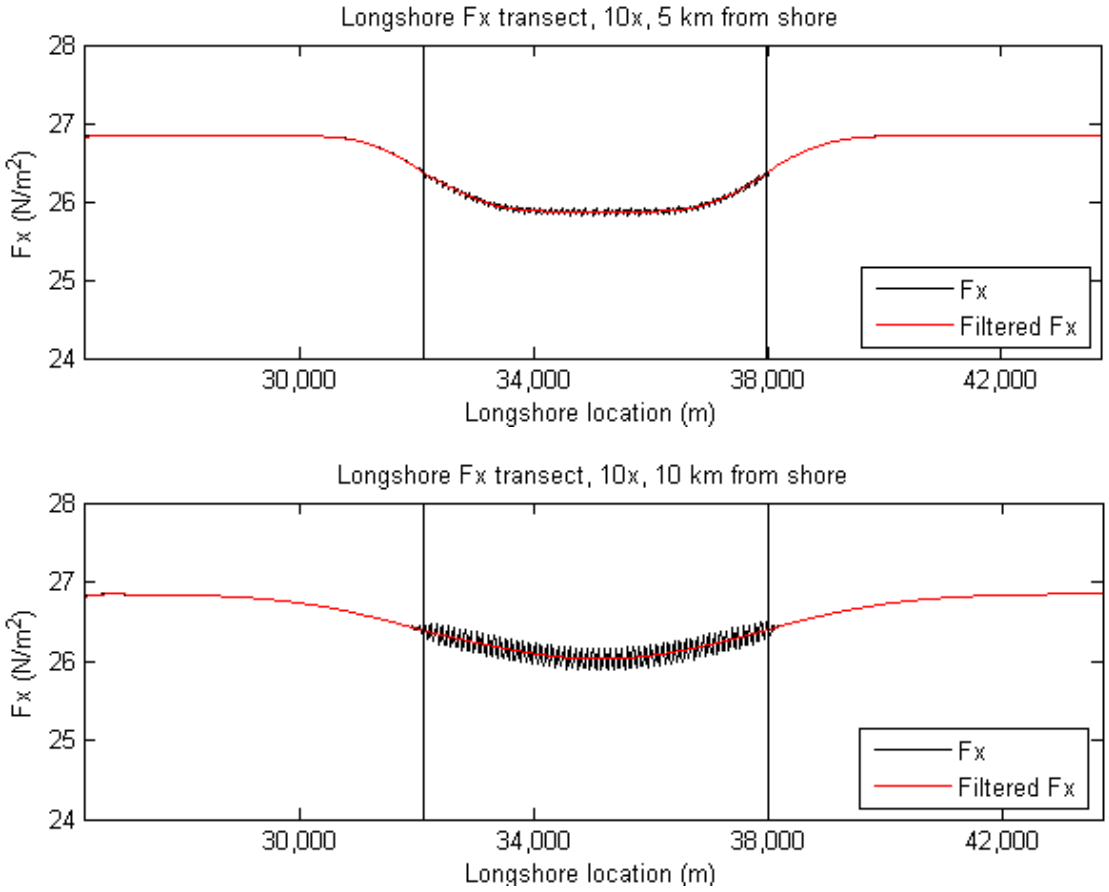

Figure 2. Longshore F_x transects in the lee of a widely-spaced array located **a)** 5 km and **b)** 10 km from shore with an input H_s = 6 m, an input T_p = 12 s, and low directional spread (14^0). The transect was taken from the location of the maximum F_x. The vertical black lines show the longshore location of the edges of the WEC array.

Appendix C: Hindcast analysis and input conditions for NNMREC trials.

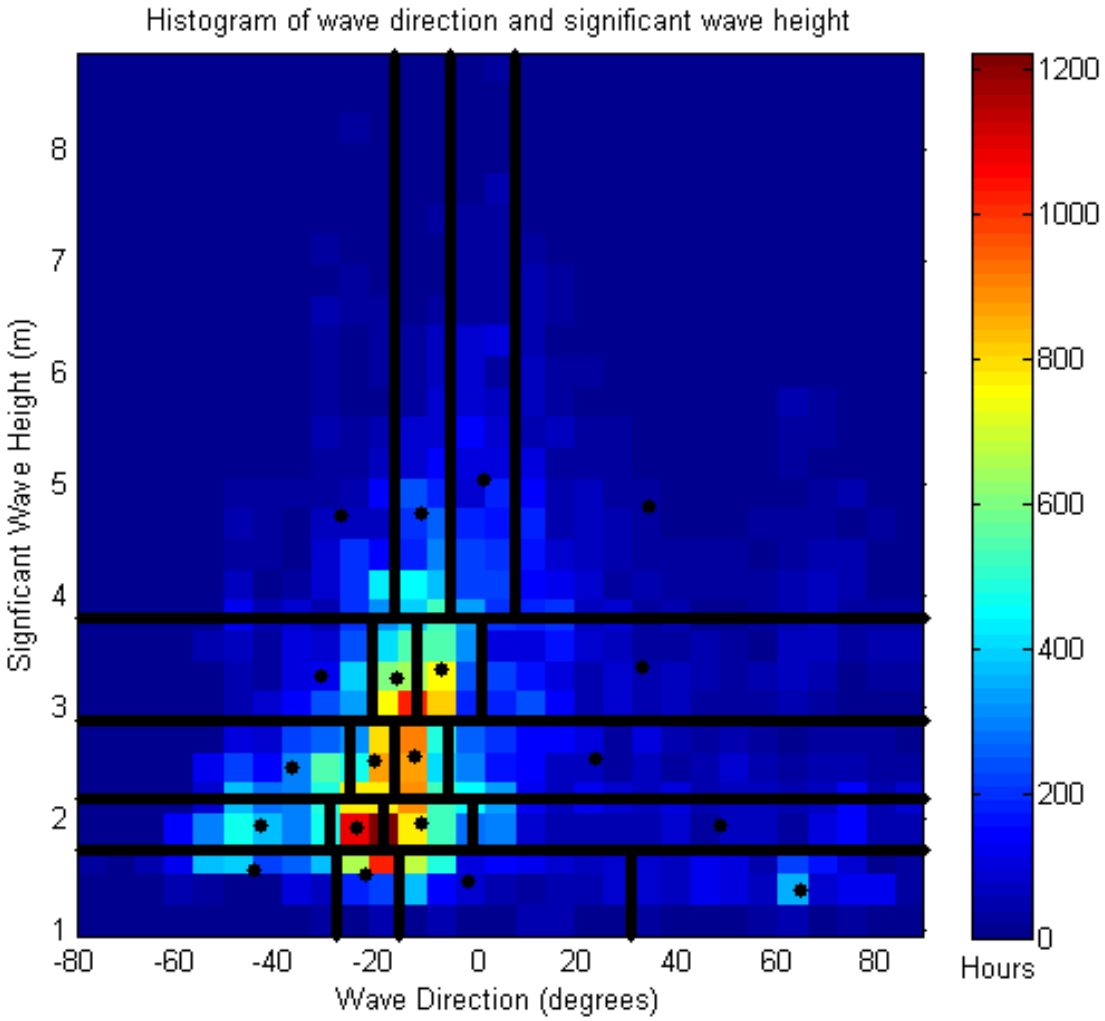

Figure 1. Two dimensional histogram of significant wave height and mean wave direction. The black lines show the bins each with an equal probability of occurrence. The centroid of each bin is shown with a black dot.

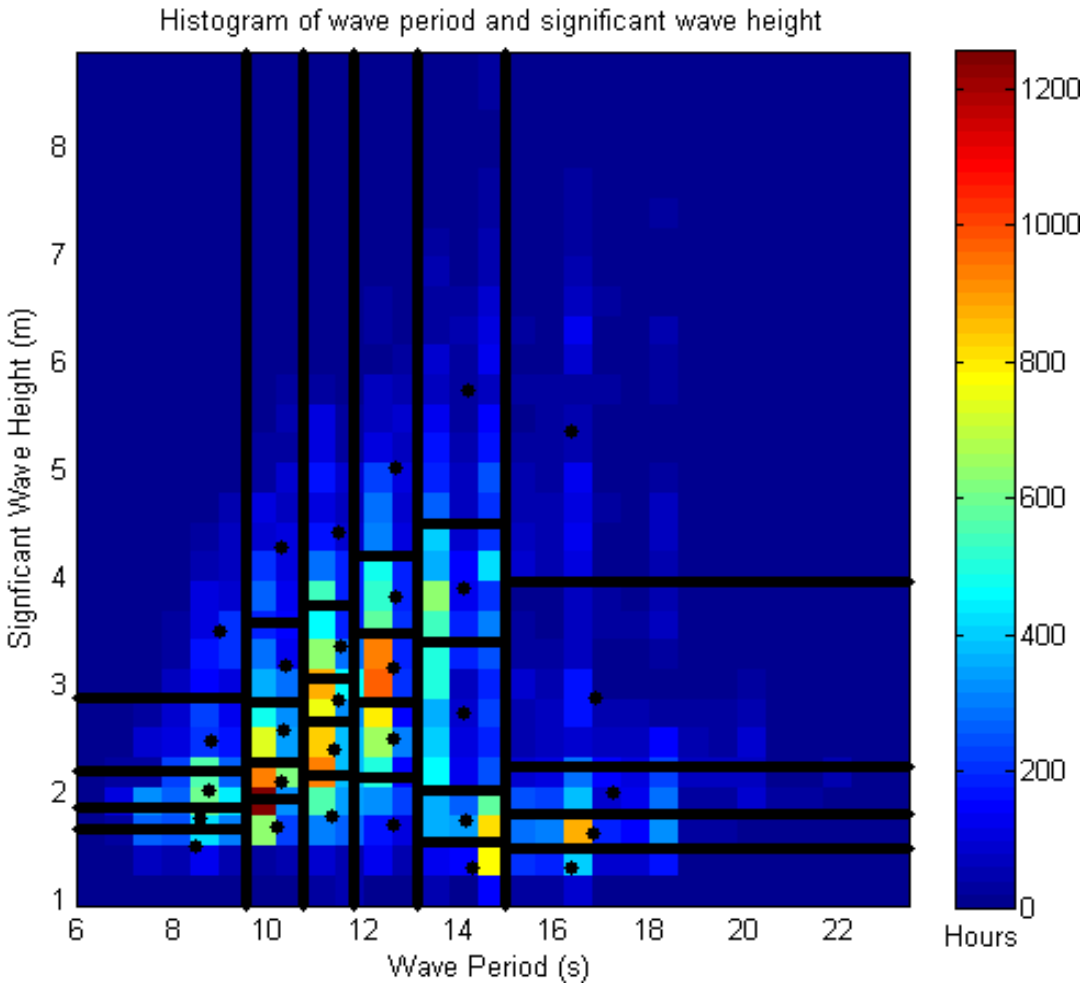

Figure 2. Two dimensional histogram of significant wave height and peak period. The black lines show the bins each with an equal probability of occurrence. The centroid of each bin is shown with a black dot.

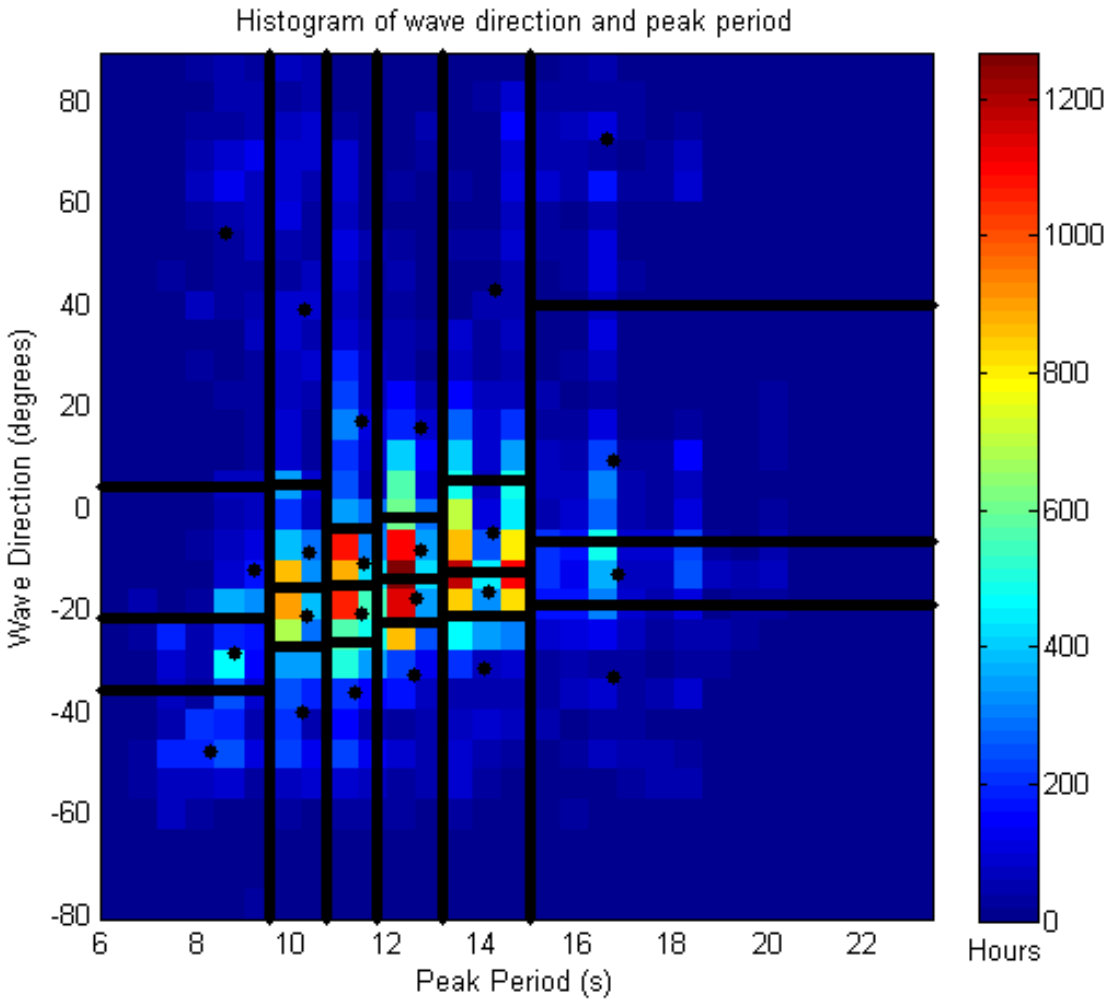

Figure 3. Two dimensional histogram of mean wave direction and peak period. The black lines show the bins each with an equal probability of occurrence. The centroid of each bin is shown with a black dot.

Table 1. Input conditions and calculated centroids for the NNMREC trials.

	Input Conditions			Calculated Centroids		
Run	**Thetap**	**Tp**	**Hs**	**Thetap**	**Tp**	**Hs**
1	-49.44	8.06	1.46	-49.55	8.05	1.52
2	-30.64	8.58	1.53	-30.59	8.24	1.47
3	-22.16	8.58	1.26	-22.18	8.71	1.47
4	2.49	8.58	1.61	-1.51	8.86	1.55
5	-52.13	8.10	1.75	-52.12	7.93	1.78
6	-32.86	8.87	1.78	-32.39	8.24	1.75
7	-22.09	9.15	1.70	-22.10	9.09	1.76
8	2.31	8.96	1.77	1.26	9.01	1.76
9	-49.31	8.17	2.15	-49.29	8.17	2.05
10	-32.67	8.58	1.94	-32.48	8.96	2.01
11	-18.74	9.52	1.97	-19.14	9.21	1.97
12	29.93	7.75	2.03	30.01	8.61	2.04
13	-49.54	8.58	2.80	-49.52	8.34	2.46
14	-34.00	9.26	2.41	-34.02	9.13	2.39
15	-7.14	9.27	2.59	-7.06	9.33	2.53
16	52.10	8.02	2.81	52.52	8.36	2.53
5	-20.80	9.21	3.35	-20.71	9.24	3.26
10	27.04	9.19	3.51	27.11	9.07	3.49
15	60.51	8.65	3.43	60.56	8.76	3.61
20	78.25	8.42	3.48	77.96	8.79	3.63
21	-47.88	10.13	1.71	-47.77	10.13	1.65
22	-25.95	10.35	1.72	-26.03	10.17	1.66
23	-19.78	10.57	1.69	-19.87	10.22	1.71
24	12.77	10.49	1.85	14.18	10.22	1.69
25	-38.49	10.09	2.06	-38.73	10.19	2.13
26	-23.27	10.21	2.22	-23.16	10.26	2.11
27	-15.26	10.20	2.09	-15.08	10.36	2.09
28	20.55	10.68	2.03	19.97	10.30	2.09
29	-35.57	10.50	2.66	-35.54	10.31	2.56
30	-21.34	10.22	2.54	-21.30	10.28	2.54
31	-11.76	10.21	2.70	-12.02	10.33	2.63
32	17.57	10.53	2.31	18.84	10.25	2.61
33	-40.65	10.04	3.56	-40.63	10.26	3.24
34	-15.99	10.57	3.12	-16.00	10.45	3.05
35	-5.73	10.57	3.24	-5.51	10.43	3.18
36	29.87	10.57	3.23	30.35	10.29	3.23
37	-34.15	10.57	4.24	-34.47	10.31	4.13
38	2.22	10.25	4.51	2.34	10.32	4.16
39	29.86	9.72	3.77	29.50	10.25	4.15
40	65.80	10.54	4.63	66.04	10.21	4.70

41	-47.85	11.47	1.66	-47.81	11.28	1.64
42	-26.67	11.24	1.81	-26.57	11.28	1.78
43	-15.24	11.38	2.14	-15.07	11.34	1.84
44	6.83	11.74	1.85	6.16	11.46	1.85
45	-30.05	11.30	2.32	-29.99	11.27	2.42
46	-18.69	11.28	2.29	-18.71	11.37	2.39
47	-11.94	11.36	2.34	-12.07	11.36	2.39
48	17.99	11.72	2.51	17.87	11.49	2.42
49	-32.50	11.36	2.94	-32.46	11.38	2.88
50	-21.92	11.29	3.02	-21.91	11.43	2.84
51	-14.73	11.49	2.69	-14.74	11.55	2.85
52	4.45	11.42	3.05	4.72	11.48	2.88
53	-35.44	11.55	3.51	-35.33	11.39	3.39
54	-19.96	11.72	3.29	-19.92	11.58	3.31
55	-10.85	11.65	3.43	-10.75	11.59	3.38
56	12.49	11.23	3.65	12.70	11.43	3.35
57	-33.69	11.11	4.22	-33.52	11.42	4.37
58	-12.50	11.72	4.17	-12.57	11.54	4.15
59	3.40	11.72	4.37	3.40	11.56	4.49
60	33.18	11.17	4.61	33.87	11.26	4.71
61	-45.83	12.49	1.84	-45.88	12.48	1.69
62	-22.33	12.46	1.68	-22.10	12.56	1.75
63	-11.92	13.02	1.66	-11.92	12.68	1.74
64	25.85	13.01	1.13	26.45	12.77	1.66
65	-30.05	12.90	2.50	-30.02	12.62	2.46
66	-19.07	12.64	2.79	-19.14	12.54	2.50
67	-12.11	12.67	2.43	-12.03	12.62	2.56
68	20.70	12.63	2.63	20.97	12.63	2.51
69	-27.92	12.30	3.43	-27.73	12.51	3.13
70	-17.71	13.01	3.10	-17.63	12.63	3.18
71	-9.29	12.83	3.37	-9.30	12.76	3.17
72	7.58	12.79	2.87	7.33	12.66	3.19
73	-29.48	12.26	3.66	-29.60	12.49	3.83
74	-16.81	12.77	3.61	-16.88	12.74	3.80
75	-9.19	13.01	3.83	-9.26	12.65	3.82
76	3.16	13.01	3.71	2.84	12.80	3.84
77	-27.11	12.61	5.45	-27.06	12.70	5.05
78	-10.83	12.25	4.54	-10.59	12.69	4.77
79	0.25	13.01	4.74	0.44	12.70	4.88
80	18.76	13.01	5.79	18.79	12.57	5.37

81	-28.71	14.04	1.19	-28.48	14.09	1.40
82	-7.40	14.44	1.31	-7.28	14.31	1.29
83	43.43	14.44	1.24	43.40	14.39	1.22
84	76.94	14.19	1.23	76.31	14.40	1.28
85	-42.95	13.85	1.71	-42.86	13.98	1.72
86	-23.77	14.44	1.65	-23.68	14.12	1.73
87	-7.62	14.44	1.56	-7.33	14.17	1.78
88	64.00	14.44	2.02	64.50	14.36	1.75
89	-26.67	13.69	2.54	-26.89	14.02	2.77
90	-17.95	14.06	2.71	-17.81	14.09	2.81
91	-12.81	14.03	2.83	-12.99	14.09	2.79
92	8.04	14.11	2.13	7.70	14.12	2.61
93	-25.70	14.15	3.68	-25.61	14.02	3.86
94	-15.93	14.06	3.75	-15.85	14.16	3.88
95	-6.91	14.15	4.06	-6.44	14.07	3.86
96	9.76	14.44	4.29	9.43	14.18	4.00
97	-28.84	14.44	5.73	-28.55	14.18	6.00
98	-13.54	14.44	5.38	-13.57	14.18	5.29
99	-3.80	14.35	6.05	-3.60	14.31	5.69
100	10.52	14.09	6.26	10.71	14.16	5.95
101	-18.49	16.02	1.29	-18.15	16.59	1.33
102	25.03	16.02	1.37	24.82	16.35	1.36
103	56.09	16.02	0.93	56.33	16.40	1.29
104	79.53	16.02	1.42	79.69	16.02	1.28
105	-41.88	16.31	1.64	-42.30	17.08	1.62
106	-18.53	15.58	1.52	-18.00	16.37	1.62
107	24.64	16.55	1.60	25.20	17.00	1.62
108	81.86	16.25	1.57	80.58	16.77	1.65
109	-40.97	16.25	2.14	-40.79	16.89	1.99
110	-16.89	17.77	2.03	-17.03	17.59	2.04
111	40.63	17.77	2.04	40.27	17.47	1.98
112	89.27	16.91	1.93	89.12	16.99	1.99
113	-32.63	15.34	2.72	-33.42	16.43	2.69
114	-18.11	17.05	2.46	-18.27	16.81	2.69
115	-13.22	17.25	2.83	-12.77	17.21	3.09
116	8.66	16.83	3.45	8.80	17.03	3.11
117	-17.71	16.02	4.61	-17.78	16.37	4.87
118	-9.91	16.02	5.16	-9.80	16.50	5.49
119	-0.98	16.02	5.42	-1.13	16.10	5.72
120	6.87	16.38	4.42	6.95	16.40	5.38

Appendix D. SWAN domain of the continental shelf, with local domain bathymetry.

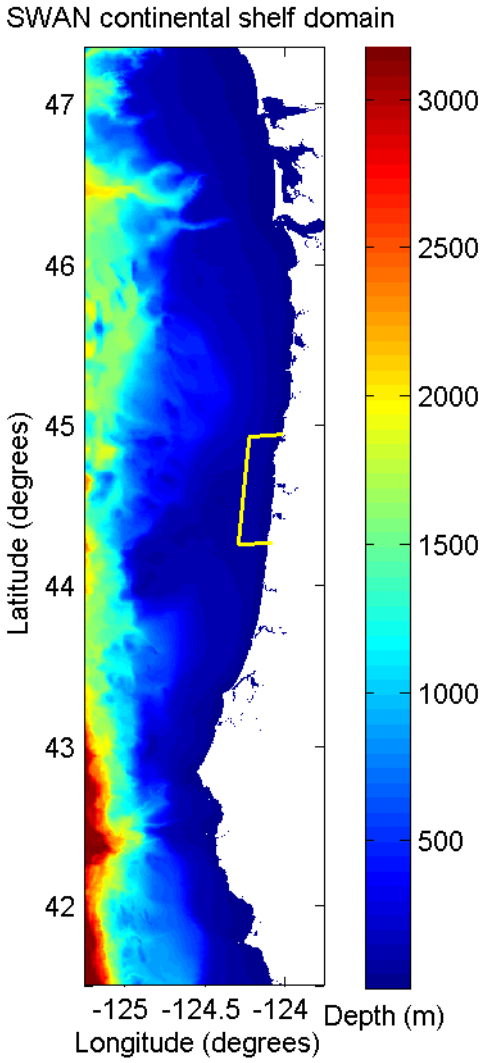

Figure 1. SWAN domain of the continental shelf. The local domain including the SETS and NETS site is shown in yellow.

Appendix E. Extended results from the study on the importance of directional asymmetry.

Table 1. Input conditions and resulting radiation stress values for all trials in the study.

	Offshore Θ (^{0})	Θ 10 m contour (^{0})	H_s at 10 m contour (m)	smax	S_{xx}/ρ (m^3/s^2)	S_{xy}/ρ (m^3/s^2)	% change S_{xx}/ρ	% change S_{xy}/ρ
NB	0	0	5.03	10	19.78	0.00		
Symmetric	0	0	5.03	10	17.71	0.00	10.47	0.00
Asymmetric	0	0	5.03	10	17.71	0.00	10.47	0.00
NB	30	16	4.78	10	16.89	3.29		
Symmetric	30	16	4.78	10	15.29	2.82	9.47	14.29
Asymmetric	30	16	4.78	10	15.68	1.90	7.16	42.25
NB	60	29	3.80	10	9.44	3.33		
Symmetric	60	29	3.80	10	8.71	3.02	7.73	9.31
Asymmetric	60	29	3.80	10	9.31	2.46	1.38	26.13
NB	0	0	5.03	75	19.78	0.00		
Symmetric	0	0	5.03	75	18.37	0.00	7.13	0.00
Asymmetric	0	0	5.03	75	18.37	0.00	7.13	0.00
NB	30	16	4.78	75	16.89	3.29		
Symmetric	30	16	4.78	75	15.70	3.08	7.05	6.38
Asymmetric	30	16	4.78	75	15.82	2.87	6.34	12.77
NB	60	29	3.80	75	9.44	3.33		
Symmetric	60	29	3.80	75	8.79	3.15	6.89	5.41
Asymmetric	60	29	3.80	75	8.93	3.05	5.40	8.41